ACSNANO

www.acsnano.org

ARTICLE

Structural Diversity in Multicomponent Nanocrystal Superlattices Comprising Lead Halide Perovskite Nanocubes

Ihor Cherniukh, Taras V. Sekh, Gabriele Rainò, Olivia J. Ashton, Max Burian, Alex Travesset, Modestos Athanasiou, Andreas Manoli, Rohit Abraham John, Mariia Svyrydenko, Viktoriia Morad, Yevhen Shynkarenko, Federico Montanarella, Denys Naumenko, Heinz Amenitsch, Grigorios Itskos, Rainer F. Mahrt, Thilo Stöferle, Rolf Erni, Maksym V. Kovalenko,* and Maryna I. Bodnarchuk*

Cite This: *ACS Nano* 2022, 16, 7210−7232

Read Online

ACCESS | Metrics & More | Article Recommendations | Supporting Information

ABSTRACT: **Nanocrystal (NC) self-assembly is a versatile platform for materials engineering at the mesoscale. The NC shape anisotropy leads to structures not observed with spherical NCs. This work presents a broad structural diversity in multicomponent, long-range ordered superlattices (SLs) comprising highly luminescent cubic $CsPbBr_3$ NCs (and $FAPbBr_3$ NCs) coassembled with the spherical, truncated cuboid, and disk-shaped NC building blocks. $CsPbBr_3$ nanocubes combined with Fe_3O_4 or $NaGdF_4$ spheres and truncated cuboid PbS NCs form binary SLs of six structure types with high packing density; namely, AB_2, quasi-ternary ABO_3, and ABO_6 types as well as previously known NaCl, AlB_2, and CuAu types. In these structures, nanocubes preserve orientational coherence. Combining nanocubes with large and thick $NaGdF_4$ nanodisks results in the orthorhombic SL resembling CaC_2 structure with pairs of $CsPbBr_3$ NCs on one lattice site. Also, we implement two substrate-free methods of SL formation. Oil-in-oil templated assembly results in the formation of binary supraparticles. Self-assembly at the liquid−air interface from the drying solution cast over the glyceryl triacetate as subphase yields extended thin films of SLs. Collective electronic states arise at low temperatures from the dense, periodic packing of NCs, observed as sharp red-shifted bands at 6 K in the photoluminescence and absorption spectra and persisting up to 200 K.**

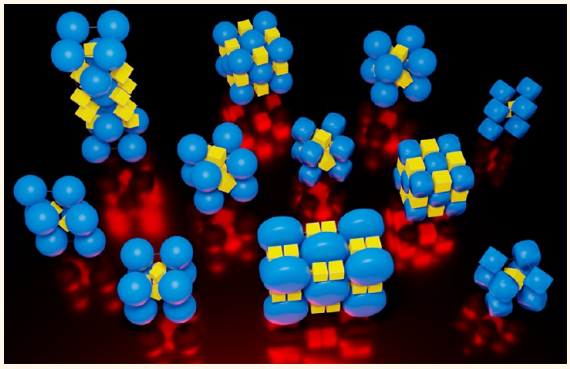

KEYWORDS: *colloidal nanocrystals, nanocrystal shape, self-assembly, binary superlattice, electron microscopy, lead halide perovskites, collective properties*

Assembly of monodisperse nanocrystals (NCs) into long-range ordered superlattices (SLs) makes an ideal platform for creating materials with controlled and programmed functionalities that result not only from the combination and enhancement of size-dependent properties of constituent building blocks but also from synergistic effects and emergent interactions between neighboring NCs.[1,2] Early examples include conductivity enhancement in binary SLs of Ag_2Te with PbTe NCs,[3] exchange coupling effects in assemblies of magnetic NCs,[4] and near-field plasmonic-plasmonic resonance in the SL comprising gold NCs.[5] Various strategies have been developed for the fabrication of single and multicomponent SL structures with desired dimensionality and geometry, including colloid destabilization by nonsolvent diffusion,[6] drying-induced assembly over tilted substrate,[7,8] or at a liquid−air interface[9−11] and microemulsion-templated assembly.[12,13] Self-organization of NCs may be further governed by the external electric and magnetic fields.[14,15] The assembly of steric-stabilized colloidal NCs coated with hydrocarbon ligand chains relies on relatively weak (van der Waals, dipole−dipole, magnetic, Coulombic) interactions between NCs[1,16] with the considerable role of entropic contributions.[7] For example, the gain in free volume entropy upon self-assembly of monodisperse spherical NCs favors the

Received: December 2, 2021
Accepted: March 31, 2022
Published: April 6, 2022

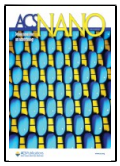

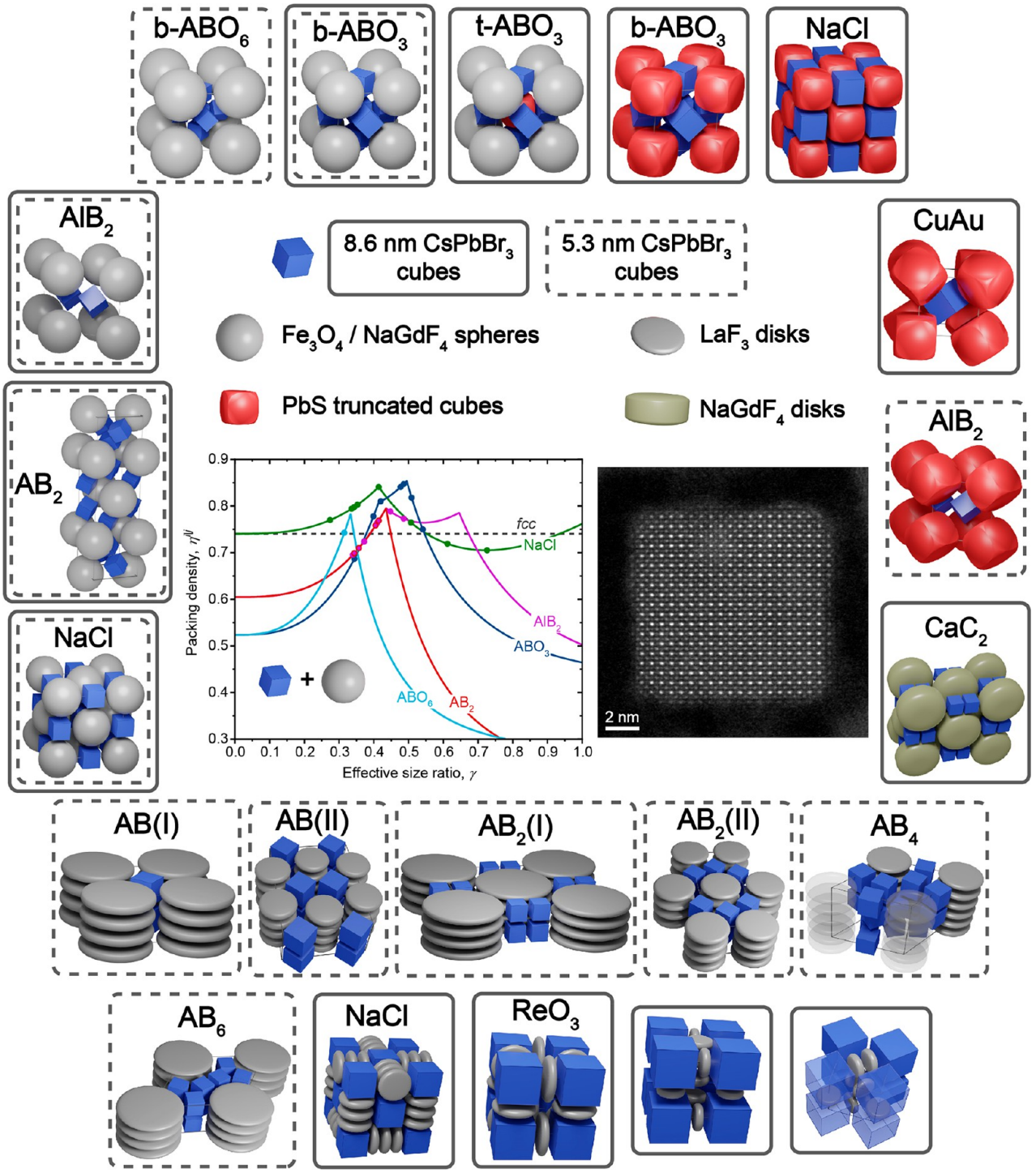

Figure 1. Diversity of binary and ternary SLs obtained from 5.3 and 8.6 nm $CsPbBr_3$ nanocubes combined with 11.2−25.1 nm spherical Fe_3O_4 and $NaGdF_4$ NCs, 10.7−11.7 nm truncated cuboid PbS NCs, thick $NaGdF_4$ disks (31.5 nm in diameter and 18.5 nm thick), and 6.5−28.4 nm disk-shaped LaF_3 NCs. Structures in solid and dashed frames were obtained with 8.6 and 5.3 nm $CsPbBr_3$ NCs, respectively. HAADF-STEM image illustrates a sharp shape of a $CsPbBr_3$ nanocube. The graph is a space-filling analysis within a hard-particle model for NaCl-, AlB_2-, and AB_2- and within OTM for ABO_3- and ABO_6-type SLs comprising larger spherical and smaller cubic NCs; the dashed line corresponds to the density of *fcc* packing of spherical NCs.

formation of the densest possible structures with face-centered cubic (*fcc*) or hexagonal close packing.[1,17] For binary mixtures of spherical NCs, over 20 structures analogous to known atomic lattices were reported. Typically, the observed structure is the one having higher packing density (η) for a given NC size ratio, $\gamma = d_B/d_A$, where d_B is the diameter of a smaller B-component and d_A is the diameter of a larger A-component, both computed taking into account the dimensions of the core and ligand shell.[2,18−20] In the simple optimal packing model (OPM),[21] the effective diameter of steric-stabilized NCs is calculated assuming that the ligand shell is space-filling along the axis connecting neighboring NCs. Commonly observed are

https://doi.org/10.1021/acsnano.1c10702
ACS Nano 2022, 16, 7210−7232

those binary SL structures, whose hard-particle packing densities are close to or exceed the packing density of *fcc* packing of spheres (η = 0.74).

Advancements in NC synthesis methodologies with exquisite NC size- and shape-engineering motivate the exploration of different SL structures.[22−24] The phase behavior of assemblies from shape-anisotropic NCs can be explained by the presence of directional entropic forces, which lead to dense local packing.[25] Already with single-component SLs of nonspherical NCs, minor differences in NC shape were reported to change the resulting structure; for instance, in the case of cubes vs truncated cubes such as Pt, PbS, or iron oxide.[26−29] A plethora of different binary SLs had been observed combining spherical NCs with several nonspherical NCs such as triangular nanoplates (columnar and three-dimensional structures),[18] nanowires and rhombic nanoplates (wherein chains of nanowires or stacked face-to-face plates template the assembly of spheres into ordered one-dimensional arrays),[30−32] nanorods (forming three-dimensional superstructures with the positional and orientational ordering of building blocks),[33,34] and branched octapod NCs.[35] Very little work has been reported for mixtures of exclusively nonspherical, anisotropic NCs. These are binary lamellar SL of shape-complementary nanoplates,[33] several columnar SLs from the mixtures of nanodisks and nanorods,[36,37] and, very recently, thin-film SLs from PbTe cubes coassembled with triangular nanoplates.[38]

Lead halide perovskite NCs—the latest generation of semiconductor quantum dots introduced in 2015[39]—have attracted much attention for their enhanced properties as narrow-band, bright light emitters[40−42] and are intensely investigated for both classical light generation (light-emitting diodes, down-conversion in LCDs)[43,44] and as single-photon sources.[45,46] Being synthetically available as sharp, monodisperse cubes with edge-length tunable in 5−20 nm,[47−49] perovskite NCs are attractive highly uniform, shape-engineered building blocks for SLs. Since 2017, $CsPbBr_3$ NCs had been reported to form superstructures with simple-cubic packing (*scp*).[50−57] At cryogenic temperatures, single-component $CsPbBr_3$ NC SLs were found to exhibit superfluorescence. There, in contrast to spontaneous emission where the individual NCs emit photons randomly and independently, a coherent coupling among several NCs in superfluorescent domains leads to collective emission, resulting in ultrafast (few tens of picoseconds) bursts of photons.[53] These findings stimulated exploration of multicomponent SLs with perovskite NCs, as a means of attaining programmable positional and orientational order of these coherent light emitters.[58,59] Fundamentally important is that these were the original trials to coassemble cubic NCs with other shapes, and the outcome was vastly different from the results of the all-sphere NC self-assembly. Specifically, when $CsPbBr_3$ nanocubes are coassembled with spherical dielectric $NaGdF_4$ NCs, the binary perovskite b-ABO_3-type SL forms, with cubes occupying B and O sites. Perovskite-type SL had not been reported, and not observed in our reference experiments, for all-sphere mixtures, which can be rationalized by much higher computed packing densities of this lattice when using cubes on B/O-sites. We then utilized the nonequivalence of B and O sites to incorporate the third component, truncated cubic PbS NCs, on a slightly larger B-site, yielding a ternary ABO_3-type SL.[58] In the subsequent work, $CsPbBr_3$ cubes were combined with thin LaF_3 disks (1.6 nm in thickness, 6.5−28.4 nm in diameter), yielding six columnar structures, wherein columns of disks and cubes form a two-dimensional periodic pattern, and four three-dimensional structures that feature face-to-face contacts between cubes and disks of comparable size.[59]

Here, we present a detailed survey and comprehensive discussion of all multicomponent SL structures (Figure 1) obtained by combining cubic $CsPbBr_3$ NCs (and $FAPbBr_3$ NCs) with diverse spherical and nonspherical NCs into multicomponent SLs. Beyond refs 58 and 59, a broader selection of building blocks was utilized (truncated cuboids and thick disks), additional structure types are presented (AB_2, b-ABO_6, CaC_2), and their formation was rationalized using space-filling calculations. Generally, cubic shape and facile ligand-deformability at the vertices and edges yield denser packing compared to spheres. In total, six structures were found in small cube-large sphere and small cube-large truncated cube mixtures, of which three are identical to those commonplace in all-sphere assemblies (NaCl, AlB_2, and CuAu types) and the other three are exclusive to the use of cubes as smaller component (AB_2, b-ABO_3, b-ABO_6). Unlike columnar structures with thin LaF_3 disks, thick $NaGdF_4$ nanodisks (18.5 nm thick, 31.5 nm in diameter) yield a CaC_2-like lattice with clusters of two 8.6 nm cubes. In all presented structures, cubic NCs are orientationally locked. While the screening of SL formation in this work and in our earlier reports (refs 58 and 59) were conducted by drying the colloids directly on the microscopy substrates, we also present the adaptation of the on-liquid formation of SLs as free-floating membranes for perovskite NCs, wherein a suited subphase solvent such as glyceryl triacetate is proposed. This polar solvent does not disperse apolar NC colloids drop-casted atop nor chemically damages the perovskite NCs. We also present the utility of the microemulsion-based method for the formation of multicomponent SLs comprising perovskite NCs. These SLs give rise to collective electronic states across perovskite NCs at low temperatures, as is evidenced by their photoluminescence (PL) and absorption spectra containing sharp red-shifted bands persisting up to 200 K.

RESULTS AND DISCUSSION

Due to rather ionic bonding and specifics of surface termination with a high propensity of lead atoms to maintain octahedral coordination, perovskite NCs tend to expose nonreconstructed, CsBr-terminated facets [(100) in pseudocubic notation], essentially without truncation.[60] Sharp nanocubes $CsPbBr_3$ with the edge lengths of 5.3 and 8.6 nm were synthesized by the hot-injection method (see respective luminescence and absorption spectra in Figure S1).[61,62] The NCs were coated by didodecyldimethylammonium bromide (DDAB), which is the shortest ligand still rendering these NCs colloidally stable. As manifested by the distinct diffraction arcs in the wide-angle selected-area electron diffraction (ED) pattern from the assembled monolayer (see Figure S2), nanocubes align face-to-face with the [001] zone axis parallel to the electron beam. $CsPbBr_3$ nanocubes crystallize in orthorhombic *Pnma* structure with six facets terminated by four {101} and two {010} planes.[60] Since the *d*-spacing between {010} and {101} planes is nearly identical, in the ED analysis we treat the structure of $CsPbBr_3$ NCs as pseudocubic with six facets terminated by {100} pseudocubic planes. 10.7 and 11.7 nm oleate-capped PbS nanocubes with truncated vertices possess rock-salt crystal structure and are terminated by {100} lattice planes. Due to similar PbS and $CsPbBr_3$ lattice

https://doi.org/10.1021/acsnano.1c10702
ACS Nano 2022, 16, 7210−7232

constants, their diffraction patterns overlap; however, because of the higher symmetry of the PbS structure, the {100} and {110} reflections are absent. The 11.2−25.1 nm Fe_3O_4 spherical NCs possessing inverse spinel cubic structure were synthesized by thermally decomposing iron oleate.[63] Spherical, 15.1−19.5 nm hexagonal-phase β-$NaGdF_4$ NCs were synthesized by thermal decomposition of gadolinium trifluoroacetate.[31] Six arcs originating from {100} lattice planes imply slight hexagonal faceting of nanospheres. The decreased sodium-to-gadolinium ratio in the precursor solution and increased reaction time lead to $NaGdF_4$ nanodisks (31.5 nm in diameter and 18.5 nm in thickness). The size distribution of NCs used in experiments was in the range from 2.9 to 7.7% [standard size deviation based on 200 particles, see transmission electron microscopy (TEM) characterization in Figure S2]. In most experiments, SLs were grown as polycrystalline films on a range of substrates (carbon-coated copper-grids and Si_3N_4 membranes on Si grids) by drying the NC mixtures in toluene.

Coassembly of $CsPbBr_3$ Cubes with Spheres. First, we will discuss the systems of cubic 8.6 and 5.3 nm $CsPbBr_3$ NCs with spherical Fe_3O_4 and $NaGdF_4$ NCs. 8.6 nm $CsPbBr_3$ nanocubes with spherical NCs can form NaCl-, AlB_2- (along with AB_2-), and b-ABO_3-type SLs, depending on particle number ratio. Figure 2a shows NaCl-type SL obtained as a

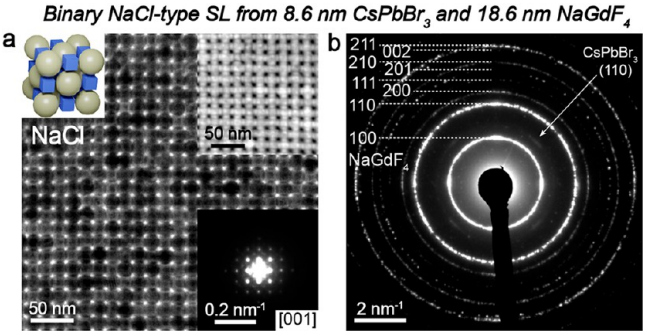

Figure 2. Binary NaCl-type SL. (a) TEM image, (upper right inset) HAADF-STEM image, along with the corresponding (bottom inset) small-angle and (b) wide-angle ED patterns of a SL domain in $[001]_{SL}$ orientation assembled from 8.6 nm $CsPbBr_3$ cubes and 18.6 nm $NaGdF_4$ NCs. The upper left inset in (a) represents the NaCl-type unit cell according to the preferential cube's orientation.

dominant product at a low $CsPbBr_3$-to-$NaGdF_4$ particle number ratio (ca. 1.2:1 and γ = 0.439). Wide-angle ED measured from a single SL domain reveals the orientation of $CsPbBr_3$ cubes with $\langle 100 \rangle$ directions coinciding with $\langle 100 \rangle_{SL}$, that is, each cube interacts with six spheres through flat facets; subscript "SL" denotes Miller indices of an SL. At high cube-to-sphere particle ratios (ca. 4.2:1), a b-ABO_3-type SL is the sole product (Figure 3a−n). In this structure, spherical Fe_3O_4 or $NaGdF_4$ NCs reside on the A site (1a position of $Pm\bar{3}m$ perovskite structure), while cubes occupy two crystallographically different sites, 1b (B site) and 3c (O sites). Distinct features of $CsPbBr_3$ in the wide-angle ED reveal the orientation of O- and B-positioned cubes: $CsPbBr_3$ NCs on faces (O-sites) interact with four spheres through facets and have two of $\langle 110 \rangle$ aligned with $\langle 100 \rangle_{SL}$, while the cube in the center of the unit cell (B-site) is 45° rotated with respect to O-cubes and has all $\langle 100 \rangle$ aligned with $\langle 100 \rangle_{SL}$ (Figure 3c,m). Scanning electron microscopy (SEM, Figure 3d,n) and atomic force microscopy (AFM, Figure e−j) illustrate the surface topology of b-ABO_3-type SLs. Precise height profile AFM measurement resolves two distinct surface terminations in $[001]_{SL}$-oriented domains: (i) spheres terminated (Figure 3e−g) and (ii) B-site cubes terminated, as evident from sharper and higher maxima in Figure 3h−j.

The formation of NaCl and b-ABO_3 SLs with cubic NCs can be rationalized by their high packing densities, exceeding those of *fcc* packing of spheres (Figure 1).[58] The coordination environment of B- and O-positioned cubes in b-ABO_3-type structure is different, for example, at $\gamma \geq 0.414$, O-cubes interact through vertices, while B-cubes are rattlers. Targeted incorporation of larger (compared to perovskite cubes) truncated cuboidal PbS NCs (11.7 nm) on B-sites leads to a three-component t-ABO_3-type SL with higher packing density than that of b-ABO_3 lattice comprising the same sizes of spheres (21.5 and 25.1 nm) and perovskite cubes (8.6 nm), Figure 3o−r. Wide-angle ED confirms the same orientation of O-site perovskite cubes as in the binary lattice, and PbS truncated cubes preserving the orientation of B-site perovskite cube. The PbS incorporation into the structure is apparent from high contrast in high-angle annular dark-field scanning TEM (HAADF-STEM) images (Figure 3p,r). The completeness of the substitution of $CsPbBr_3$ cubes on B site by PbS NCs is evident from the absence of (110) reflection ("1" in Figure 3q) expected from the center perovskite cube, while the (220) reflection originating from PbS ("2" in Figure 3q) is intensely diffracting in the analogous direction. These structures are also described in our previous work, ref 58.

At the intermediate particle number ratios (ca. 2.2:1, cubes-to-spheres), the dominant product is an AlB_2-type SL. Figure 4a−e shows TEM characterization of $[120]_{SL}$-oriented domain assembled from 8.6 nm $CsPbBr_3$ and 19.8 nm Fe_3O_4 NCs, while Figure 4f−j presents $[001]_{SL}$-oriented domain obtained from 8.6 nm $CsPbBr_3$ combined with 16.5 nm $NaGdF_4$ NCs. In this lattice, nanocubes occupy each trigonal prismatic void in a simple hexagonal lattice of spheres. Wide-angle ED pattern from $[120]_{SL}$-oriented domain (Figure 4e) comprises narrow arcs originating from (110) and (111) $CsPbBr_3$ lattice planes that run in perpendicular directions, while the ED pattern from $[001]_{SL}$ projection (Figure 4j) features six (110) $CsPbBr_3$ arcs at 60° angles. This is reflective of the preferential orientation of $CsPbBr_3$ nanocubes in the SL: one of their [111] directions is aligned with $[001]_{SL}$ (6-fold axis) and [110] with $[010]_{SL}$, that is, cubes interact with three spheres from one side of the trigonal prismatic void via facets and with three spheres from another side via edges.

Smaller, 5.3 nm $CsPbBr_3$ nanocubes with Fe_3O_4 NCs readily form NaCl- (Figure S3) and AlB_2-type SLs, in which, similar to larger cubes, a high degree of orientational order is observed. AlB_2-type binary SLs are obtained with iron oxide NCs (11.2−15.6 nm, γ = 0.443, 0.405, 0.368, 0.336, Figure 5 and Figure S4). Structural peculiarities of the AlB_2 binary SL are detailed here for the case of 12.5 nm Fe_3O_4 NCs (Figure 5). The grazing-incidence small-angle X-ray scattering (GISAXS) pattern shows strong, periodic reflections (Figure 5c) owing to long-range order and complex, base-centered orthorhombic symmetry (*C*222), resulting from the stacking of hexagonal $CsPbBr_3$ and Fe_3O_4 layers, with an in-plane A−B−A−B packing direction, as also confirmed by energy-dispersive X-ray spectroscopy (EDX-STEM, on Figure 5g). See Supplementary Note 1 and Figure S5 for further details on GISAXS SL

https://doi.org/10.1021/acsnano.1c10702
ACS Nano 2022, 16, 7210−7232

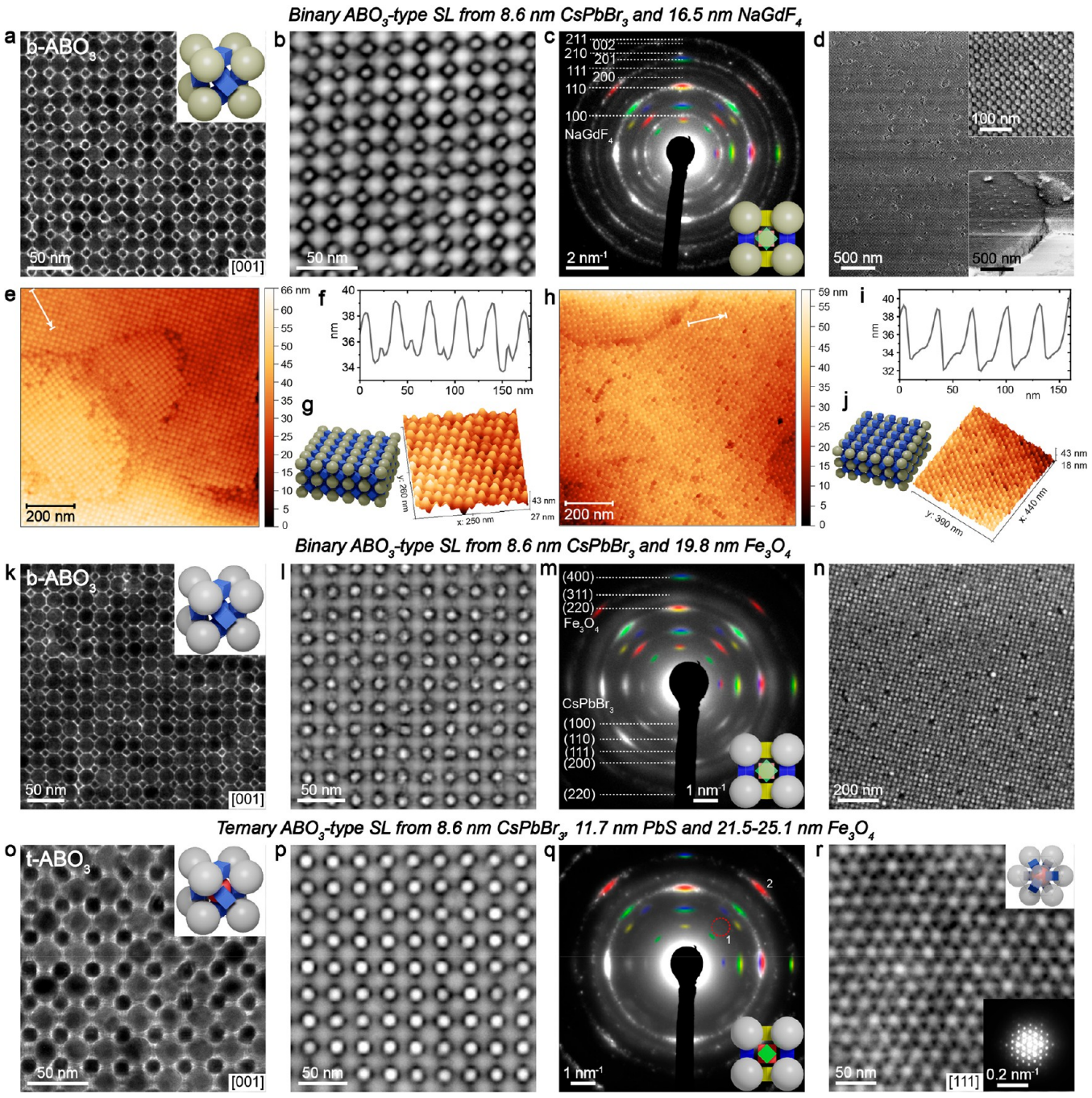

Figure 3. Binary and ternary ABO_3-type SLs. (a) TEM image along with (b) HAADF-STEM image, (c) the corresponding wide-angle ED pattern, and (d) SEM images of the $[001]_{SL}$-oriented b-ABO_3-type domains assembled from 8.6 nm $CsPbBr_3$ cubes and 16.5 nm $NaGdF_4$ spheres. (e, h) AFM height images of spheres- and cubes-terminated b-ABO_3-type domains, respectively, along with (f, i) the height analysis of the profiles indicated in (e, h), (g, j) AFM three-dimensional images with the respective models. (k) TEM image along with (l) HAADF-STEM image, (m) the corresponding wide-angle ED pattern, and (n) SEM image of the $[001]_{SL}$-oriented b-ABO_3-type domains assembled from 8.6 nm $CsPbBr_3$ cubes and 19.8 nm Fe_3O_4 spheres. (o) TEM image along with (p) HAADF-STEM image and (q) the corresponding wide-angle ED pattern of the [001]-oriented t-ABO_3-type SL domains assembled from 8.6 nm $CsPbBr_3$ cubes, 11.7 nm PbS truncated cuboids, and 21.5 nm Fe_3O_4 spheres. (r) HAADF-STEM image of a t-ABO_3-type SL domain in $[111]_{SL}$ orientation assembled from 8.6 nm $CsPbBr_3$, 11.7 nm PbS, and 25.1 nm Fe_3O_4 NCs; upper inset shows the model of $[111]_{SL}$-oriented t-ABO_3 unit cell, and lower inset shows small-angle ED pattern. Insets in (a, k, o) represent binary and ternary ABO_3-type lattices according to the preferential NCs orientations, with Fe_3O_4 shown as gray spheres, $NaGdF_4$ as yellowish spheres, $CsPbBr_3$ as blue cubes, and PbS as red truncated cubes. The origin of wide-angle ED reflections in (c, m, q) is color-coded to match the NCs in insets.

characterization. TEM tilting series readily differentiate the predominantly observed $[120]_{SL}$ projection of the AlB_2-type from the similar $[100]_{SL}$ projection of CuAu-type SL (Figure S6). The AlB_2-type structure was additionally confirmed by electron tomography of $[001]_{SL}$-oriented domain (see Supplementary Video 1). Figure 5i–n displays occasionally observed $[001]_{SL}$ and $[010]_{SL}$ projections of AlB_2-type SL. The signal-to-noise ratio was improved upon template matching

https://doi.org/10.1021/acsnano.1c10702
ACS Nano 2022, 16, 7210–7232

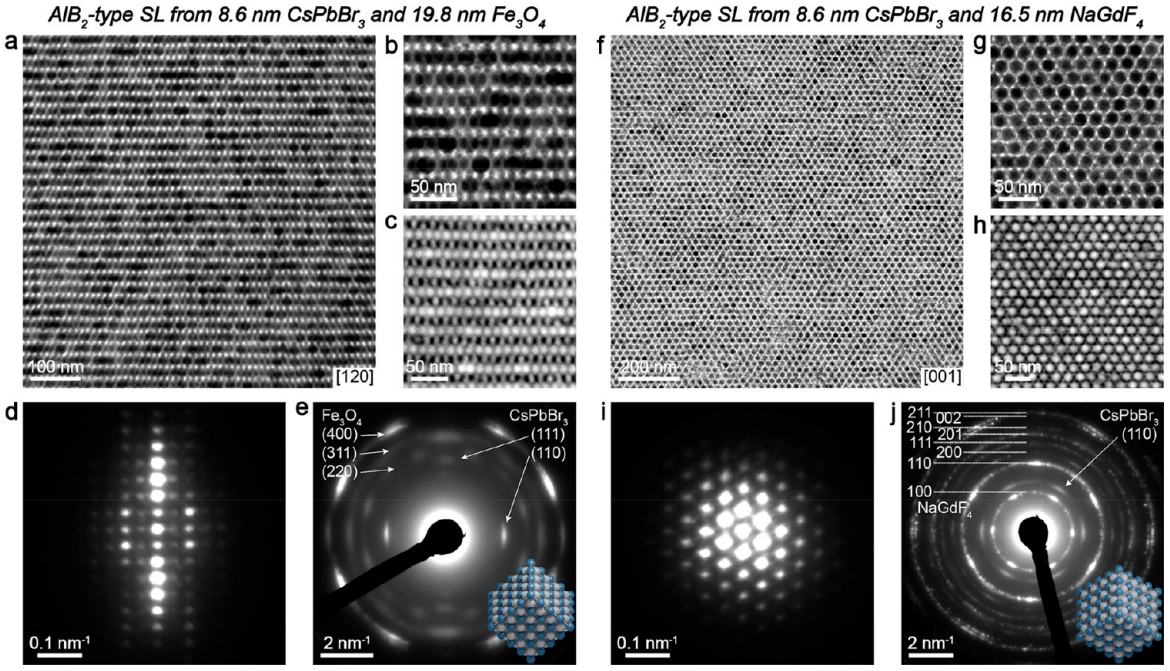

Figure 4. Binary AlB_2-type SLs obtained combining 8.6 nm $CsPbBr_3$ with (a−e) 19.8 nm Fe_3O_4 and (f−j) 16.5 nm $NaGdF_4$ NCs. (a, b) TEM and (c) HAADF-STEM images of a single domain in $[120]_{SL}$ orientation, along with the corresponding (d) small-angle and (e) wide-angle ED patterns. (f, g) TEM and (h) HAADF-STEM images of a single domain in $[001]_{SL}$ orientation, along with the corresponding (i) small-angle and (j) wide-angle ED patterns. Insets in (e, j) show the orientations of $CsPbBr_3$ NCs in the SL domains with respect to the electron beam (normal to the image plane).

and averaging of large homogeneous areas of TEM images (insets in Figure 5i,l). Small-angle ED and wide-angle ED patterns (for $[120]_{SL}$-orientation) confirm the preferential orientation of nanocubes analogously to AlB_2-lattices with larger $CsPbBr_3$ NCs, albeit with much weaker intensities of perovskite reflections due to reduced scattering factor of small NCs. The broader arcs indicate a higher orientational freedom of smaller nanocubes within the SL. The (111) and (110) lattice planes of $CsPbBr_3$ are normal to $[001]_{SL}$ and $[010]_{SL}$, respectively, as in the binary SLs with larger cubes. However, there are three sets of {110} $CsPbBr_3$ lattice planes with a common [111] zone axis that is parallel to $[001]_{SL}$. Therefore, 60° rotation around $[001]_{SL}$ does not change the position of diffraction spots. Consequently, there are two possible relative orientations of nanocubes: half of the cubes being 60° rotated about $[001]_{SL}$ ("O1") or all having the same orientation ("O2", Figure 6a). We would also note that ambiguity in this rotational orientation around $[001]_{SL}$, as well as the possibility of the partial rattling of cubes along the same direction (not resolvable with TEM images), complicates the packing density analysis (Figure 6b). Our analysis shows that a combined effect of the "O2"-orientation and cube displacement along $[001]_{SL}$ direction can lead to the hard-particle packing densities of 0.7−0.8 in the γ range of 0.35−0.70 (see detailed discussion and calculations in the Supplementary Note 2).

Next to AlB_2-type binary SLs and for both sizes of nanocubes combined with Fe_3O_4 spheres, another AB_2 structure belonging to the tetragonal crystal system, namely the $P4_2/mmc$ space group, concomitantly forms (Figure 7 and Figures S8−S10). This structure can be viewed as derived from the AlB_2 structure with a small modification: Shifting of each fourth (100) lattice plane along [011] vector, the corresponding lattice plane and the direction of shifting are marked in Figure 7d. This AB_2-type packing is characterized by spherical NCs forming trigonal prisms, highlighted in Figure 7d, alternating in two perpendicular directions normal to the out-of-plane $[001]_{SL}$, with cubic NCs occupying each void orienting in the same way as in the trigonal prismatic void of AlB_2-type lattice, hence retaining the AB_2 stoichiometry. Such ordering is in agreement with the contrast differences in TEM, HAADF-STEM images, EDX elemental mapping, and wide-angle ED patterns of $[001]_{SL}$ projection (Figure 7 and Figures S9 and S10). Its wide-angle ED displays reflections originating from (110) and (111) $CsPbBr_3$ lattice planes (four arcs of each kind) running normal to $[100]_{SL}$ and $[010]_{SL}$, which implies two relative orientations of nanocubes with a 90° angle between [111] directions because reflections from (110) and (111) planes of one nanocube cannot appear in the same direction. The higher yield of AlB_2-type SLs indicates its lower formation energy barrier compared to AB_2 SLs, while the calculated packing densities of both structures coincide up to $\gamma \leq 0.435$ (see for details Supplementary Note 3 and Figure 1 and Figure S8).

At $\gamma = 0.315$ (5.3 nm $CsPbBr_3$ and 16.9 nm Fe_3O_4 NCs) and high cube-to-sphere particle number ratio (ca. 12:1), binary b-ABO_6-type SL forms (Figure 8). It possesses a $Pm\bar{3}m$ space group with cubic NCs occupying one B-site (1b Wyckoff position) and six O-sites (6f Wyckoff position). This structure can also be viewed as ABO_3-like, where each of three O-sites (3c Wyckoff position) are occupied by two small cubes. O-positioned cubes are well resolved in HAADF-STEM images of $[111]_{SL}$-, $[101]_{SL}$-, and, especially, $[001]_{SL}$-oriented domains (Figure 8d−g). Higher intensity of four {110} $CsPbBr_3$ arcs in the wide-angle ED is in agreement with the alignment of the majority of cubes (O-sites) with two of ⟨110⟩ crystallographic directions pointing along with two $\langle 100 \rangle_{SL}$; however, their broadening may indicate lower orientational order. Space-filling analysis within the hard-particle model revealed a narrow

https://doi.org/10.1021/acsnano.1c10702
ACS Nano 2022, 16, 7210−7232

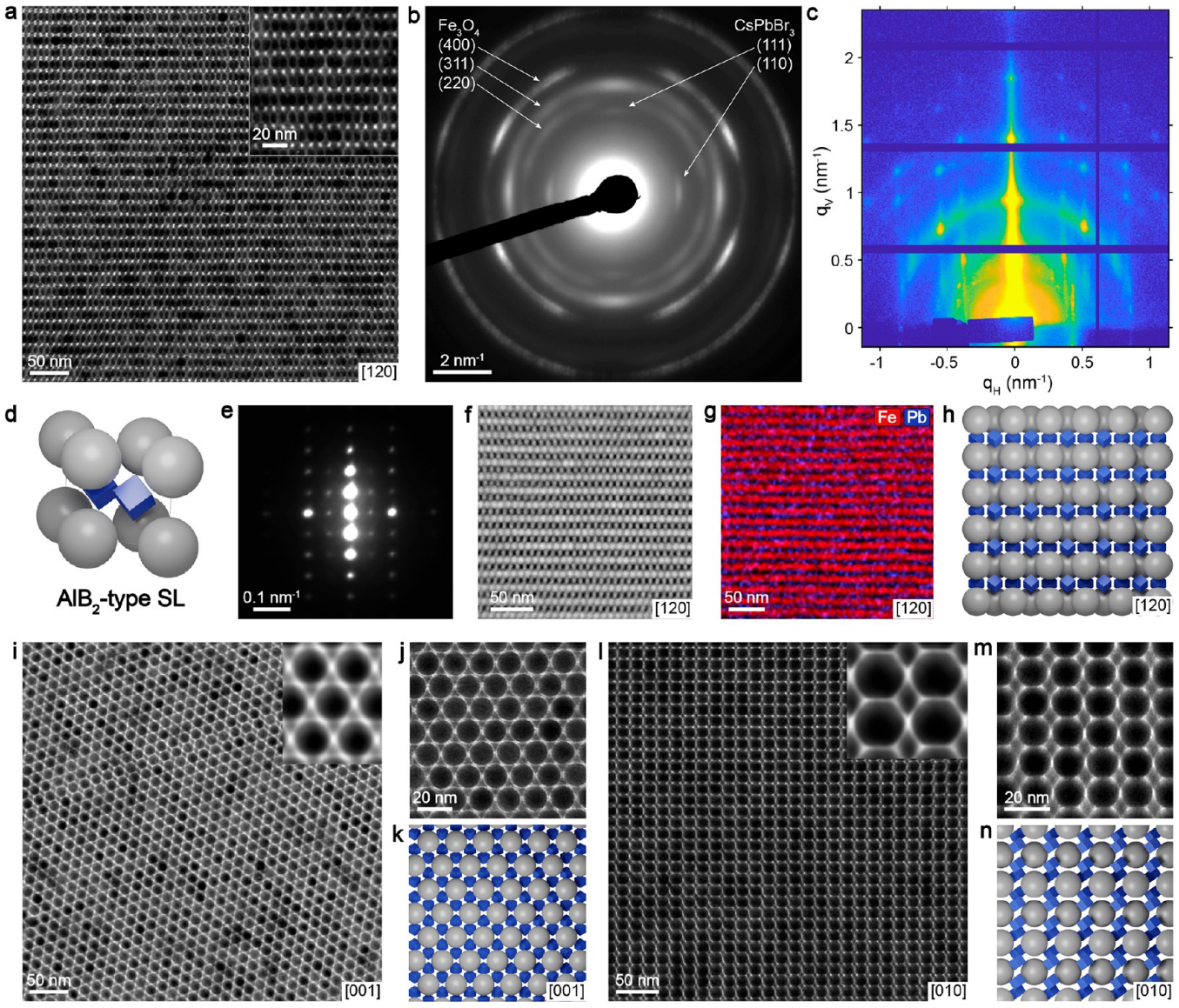

Figure 5. Structural characterization of a binary AlB_2-type SL comprising 5.3 nm $CsPbBr_3$ and 12.5 nm Fe_3O_4 NCs. (a) TEM image of $[120]_{SL}$-oriented domain; inset is the image at higher magnification. (b) Wide-angle ED pattern of a single SL domain in (a). (c) Two-dimensional GISAX scattering pattern, showing long-range order in AlB_2-type binary domains. (d) The unit cell of AlB_2-type SL. (e) Small-angle ED pattern of a domain shown in (a). (f) HAADF-STEM image of the $[120]_{SL}$-oriented domain. (g) EDX-STEM maps for Fe (gray, K-line) and Pb (blue, L-line) of the $[120]_{SL}$-oriented domain. (h, k, n) Crystallographic models of $[120]_{SL}$, $[001]_{SL}$, and $[010]_{SL}$-oriented AlB_2 lattice, respectively. (i, j) Low- and high-magnification TEM images of an $[001]_{SL}$-oriented domain. (l, m) Low- and high-magnification TEM images of a $[010]_{SL}$-oriented domain; insets in (i, l) are images obtained by template-matching analysis of corresponding TEM images.

maximum which is still below the *fcc* limit (Figure 8b). Consideration of the deformability of ligand shell on cubic NCs contacting through vertices, within orbifold topological model[64] (OTM, see calculations in the Supplementary Note 4), results in the densification of the lattice and may explain its formation within a narrow size ratio range as such lattice was not observed with 19.8 and 15.6 nm Fe_3O_4 NCs.

The usage of 15.2 nm $NaGdF_4$ NCs as spherical building blocks in coassembly with 5.3 nm $CsPbBr_3$ nanocubes (γ = 0.344) results in the formation of NaCl-, AlB_2-, and AB_2-type SLs with orientationally aligned perovskite nanocubes (Figure 9a–l), analogously to the case of Fe_3O_4 spheres. We also observed the formation of b-ABO_3-type SL at a high cube-to-sphere particle number ratio in the solution (Figure 9m,n). Interestingly, as evident from distinct arcs in wide-angle ED, a high degree of orientational ordering of A-site NCs was observed in all these structures, especially in AlB_2- and AB_2-types featuring hexagonal motifs, further pointing to the hexagonal faceting of $NaGdF_4$ NCs. Specifically, in NaCl-type SL, the (100) lattice planes tend to align normally to the in-plane $\langle 110 \rangle_{SL}$. At $\gamma < 0.414$, NaCl-type SL is defined by the *fcc* sublattice of A-particles with cubes rattling in the voids and neighboring $NaGdF_4$ NCs prefer to interact through the surfaces faceted by (100) and (001) planes. Interestingly, at $\gamma > 0.414$ (see Figure 2a,b for γ = 0.439), when A-particles contact O-cubes, the preferred orientation of $NaGdF_4$ NCs is different, they orient faceted surfaces toward cube facets, as manifested by a higher intensity of (100) and (002) wide-angle ED reflections along $\langle 100 \rangle_{SL}$. In AlB_2-type SL, $NaGdF_4$ NCs within one hexagonal layer contact each other predominantly

https://doi.org/10.1021/acsnano.1c10702
ACS Nano 2022, 16, 7210–7232

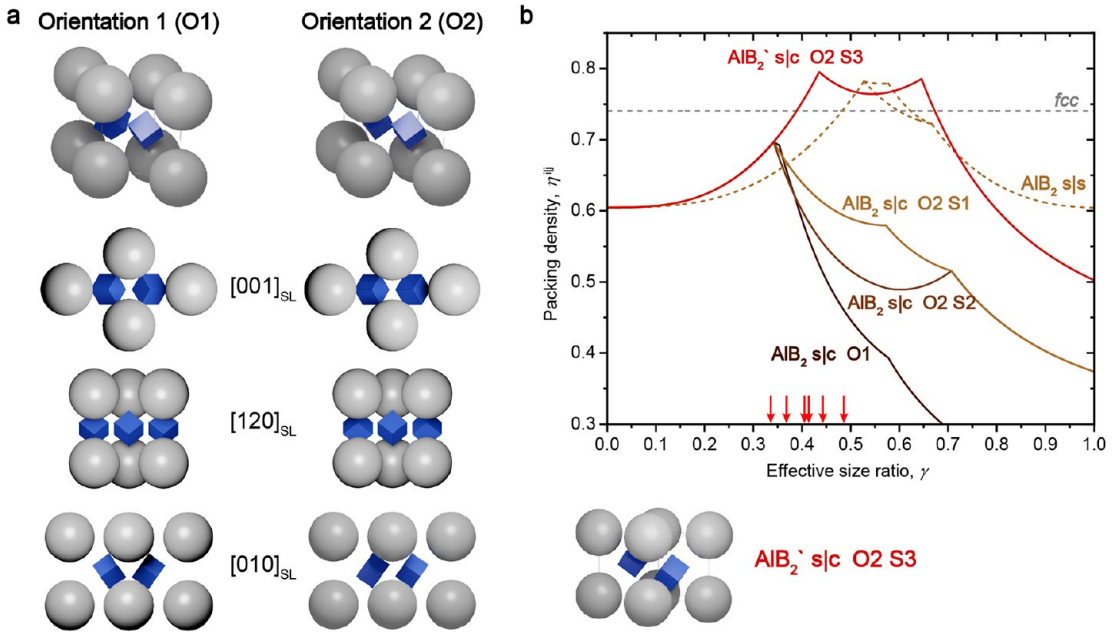

Figure 6. Possible relative orientations of $CsPbBr_3$ nanocubes within AlB_2-type SL and packing fractions predicted by OPM packing analysis according to the hard-particle model. In both orientations, the body-diagonal of the cubes is parallel to the *c*-axis of the hexagonal SL unit cell, that is, $[001]_{SL}$. In orientation "O1", the cubes are mutually rotated by 60°, whereas in orientation "O2", they are identically aligned. A significant increase in the packing fraction can be achieved if the B-cubes in orientation "O2" are not locked in the 2d Wyckoff positions, that is, are allowed to slide along the $[001]_{SL}$ ("O2 S3"). Wide-angle ED patterns from $[120]_{SL}$- (see, for instance, Figures 4e and 5b) and $[001]_{SL}$-oriented domains (Figure 5j) point to the alignment of all cubes with one body diagonal parallel to $[001]_{SL}$ and (110) $CsPbBr_3$ planes are orthogonal to $[010]_{SL}$. Hence these two orientations can be proposed. Experimentally, however, there exists no evidence to differentiate between these two structures, and hence both were considered for the analysis of lattice parameters and packing densities. Excluded is also a substantial orientational disorder in any dimension.

through the surfaces terminated by (100) planes and contact A-particles from other layers by (001) terminated surfaces, as is evident from six sharp (100) diffraction spots measured from $[001]_{SL}$-oriented domain and from the sets of (100) and (002) narrow arcs originating along $[010]_{SL}$ and $[001]_{SL}$ directions, respectively, measured from $[120]_{SL}$-oriented domain (Figure 9f,h). The wide-angle ED pattern measured from $[001]_{SL}$-oriented AB_2-type domain (Figure 9j) consists of two sets of the $NaGdF_4$ reflections present in the pattern of $[120]_{SL}$-oriented AlB_2-type domain (Figure 9h) rotated by 90°, completely in agreement with the proposed AB_2 structure in Figures 7d and 9o. The formation of b-ABO_3-type SL can benefit from the patchiness of $NaGdF_4$ NCs,[65] as in this structure, which at $\gamma < 0.414$ is governed by contacts between A-particles in *scp*, $NaGdF_4$ NCs orient their surfaces faceted by (100) and (001) planes along $[100]_{SL}$ and $[110]_{SL}$ in-plane directions.

Coassembly of $CsPbBr_3$ Cubes with Truncated Cuboids. We then studied the assembly behavior of the system comprising $CsPbBr_3$ cubes and truncated cuboid PbS NCs. Intriguingly, truncated cubes can behave similarly to spheres and occupy A-sites in binary ABO_3- and NaCl-type SLs, albeit losing orientational freedom. The b-ABO_3-type SLs form from the mixtures of 8.6 nm $CsPbBr_3$ nanocubes with 10.7−11.7 nm truncated cubic PbS NCs (Figure 10). The corresponding size ratios (γ = 0.72−0.78) are much higher compared to the systems with spherical NCs as an A-component wherein b-ABO_3-type SL forms up to γ = 0.54. EDX-STEM maps confirm that PbS NCs occupy only A-sites. Eight (100) and (110) maxima which appear in the directions normal to $\langle 100\rangle_{SL}$ and $\langle 110\rangle_{SL}$ together with eight (111) maxima with a splitting angle of 19.5° in wide-angle ED pattern indicate the presence of B- and O-positioned $CsPbBr_3$ cubes with the same orientations as in the b-ABO_3-type SLs comprising spheres on A-sites. Moreover, as can be seen from TEM image and wide-angle ED analysis, namely the higher intensity of the reflections "2" and "3" which originate mainly from strongly diffracting PbS NCs compared to the intensity of the reflections "1" and "4" which are produced only by $CsPbBr_3$ NCs, the orientation of PbS NCs is not random and matches the orientation of O-site $CsPbBr_3$ nanocubes residing on the unit cell faces parallel to the substrate. Such PbS orientation implies contacts between PbS vertices and faces of the other O-site cubes residing on perpendicular to the substrate facets of ABO_3 lattice (see insets in Figure 10a,d), making the truncated shape of larger cubes beneficial for the formation of b-ABO_3 structure. For example, such a structure could not be obtained from the binary mixtures of sharp cubic $CsPbBr_3$ NCs of two sizes.

At lower $CsPbBr_3$ loading, the dominant product is NaCl-type SL which is characterized by the alignment of ⟨100⟩ directions of both $CsPbBr_3$ and PbS NCs coinciding with $\langle 100\rangle_{SL}$, as is evident from ED. Figure 11a−c shows TEM and HAADF-STEM images of binary domains with gradually increasing thickness, in agreement with the vanishing difference in intensities of neighboring SL site projections of NaCl-type SL. A much higher wide-angle ED intensity of (200) and (220) peaks compared to that of (100) and (110) results from stronger scattering on PbS lattice planes, which contribute only to the former set of reflections and do not to the latter due to higher $Fm\bar{3}m$ symmetry of the PbS lattice; furthermore, (200)

https://doi.org/10.1021/acsnano.1c10702
ACS Nano 2022, 16, 7210−7232

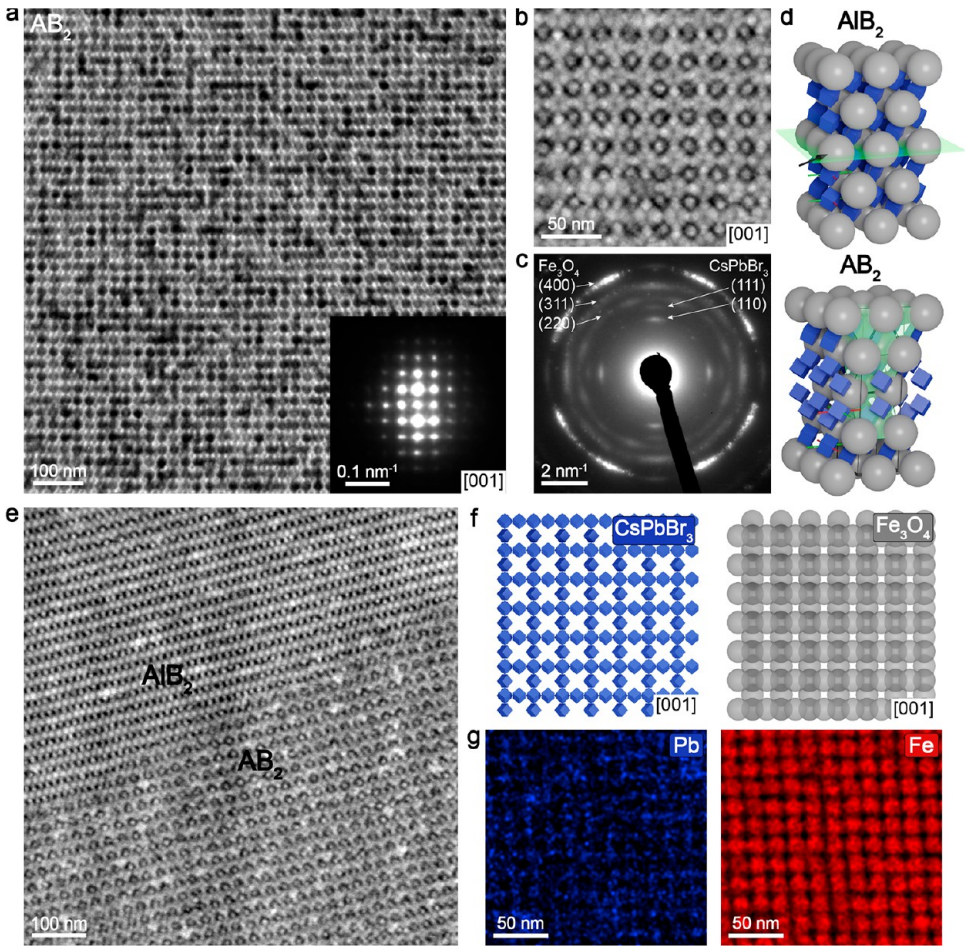

Figure 7. An AB_2-type binary SL assembled from $CsPbBr_3$ nanocubes and Fe_3O_4 nanospheres. (a) TEM image of a SL assembled by 8.6 nm $CsPbBr_3$ and 19.8 nm Fe_3O_4 NCs (γ = 0.414), along with the corresponding (inset) small-angle ED pattern, (b) HAADF-STEM image, and (c) wide-angle ED pattern. (d) Comparison of AlB_2 (taken as orientation "O2", see Figure 6) and AB_2 structures. Red and green lines show the normals to (111) and (110) $CsPbBr_3$ lattice planes, respectively, and indicate the directions of reflections in wide-angle ED patterns. (e) HAADF-STEM image showing grain boundary between AlB_2 and AB_2 binary SL domains. (f) Modeled crystallographic projections of cubic and spherical NCs in AB_2 structure. (g) EDX-STEM elemental maps of an AB_2-type binary SL assembled from 5.3 nm $CsPbBr_3$ and 14.5 nm Fe_3O_4 NCs for Pb (blue, L-line) and Fe (red, K-line).

and (220) reflections from PbS and $CsPbBr_3$ add up due to similar lattice constants (Figure 11g and Figure S11).

The 8.6 nm $CsPbBr_3$ cubes with 10.7 nm PbS truncated cubes also form a CuAu-type SL (Figure 12a–f). Typically observed is the $[101]_{SL}$ orientation (Figure 12a). The site occupancies are confirmed by recording HAADF-STEM images of $[101]_{SL}$-oriented domains at 0° and 45° tilting angles and comparing them with the modeled CuAu projections (Figure 12d,e). Complex wide-angle ED pattern (Figure 12b), contrary to b-ABO_3- and NaCl-type SLs, reveals several different orientations of PbS cuboids that reside on equivalent lattice sites. Similar orientational behavior of PbS NCs is observed in AlB_2-type SL assembled from 5.3 nm $CsPbBr_3$ NCs (Figure 12g–i). The $[010]_{SL}$ and $[001]_{SL}$ orientations that are common to AlB_2-type SLs from all-sphere systems were observed (Figure 12g), while the dominant one was $[120]_{SL}$. In this lattice, the majority of PbS NCs are aligned with [110] along $[120]_{SL}$ and [100] along $[010]_{SL}$; however, several distinct peaks remain undefined. Weak $CsPbBr_3$ (110) arcs indicate that perovskite cubes orient one edge along $[010]_{SL}$, yet the intense (111) reflections from PbS NCs hinder the determination of $CsPbBr_3$ (111) peaks, and, consequently, the conclusion whether cube orientation is the same as in the AlB_2-type SL with spherical NCs on the A-site.

Coassembly of $CsPbBr_3$ Cubes with Thick Nanodisks. Combining 8.6 nm perovskite nanocubes with larger $NaGdF_4$ disks (31.5 nm in diameter and 18.5 nm in thickness) resulted in the formation of an SL structure featuring the periodic clustering of two $CsPbBr_3$ NCs, which we interpret as a CaC_2-like SL (Figure 13), albeit with an orthogonal unit cell metric due to anisotropic shape of the $NaGdF_4$ NCs. SEM images of the surface of SL domains (Figure 13d,e) show the occupancy of one lattice site by pairs of cubes with face-to-face alignment. Within one layer, cubes are surrounded by four vertically oriented disks, two of which approach cubes by flat faces and the other two by their rims. Nanodisks from the next layer assemble on top of cubes from the previous layer, emulating the CaC_2-like packing. Such ordering is in agreement with the contrast observed in TEM of the monolayer domain (Figure S12) and TEM and HAADF-STEM image of multilayer (Figure 13a,b) and was unambiguously confirmed by electron tomography reconstruction of ordered SL domains (see Supplementary Video 2). Four narrow arcs from (100) and (110) $CsPbBr_3$ lattice planes in the wide-angle ED reveal the orientation of perovskite cubes, pointing their faces along three

https://doi.org/10.1021/acsnano.1c10702
ACS Nano 2022, 16, 7210–7232

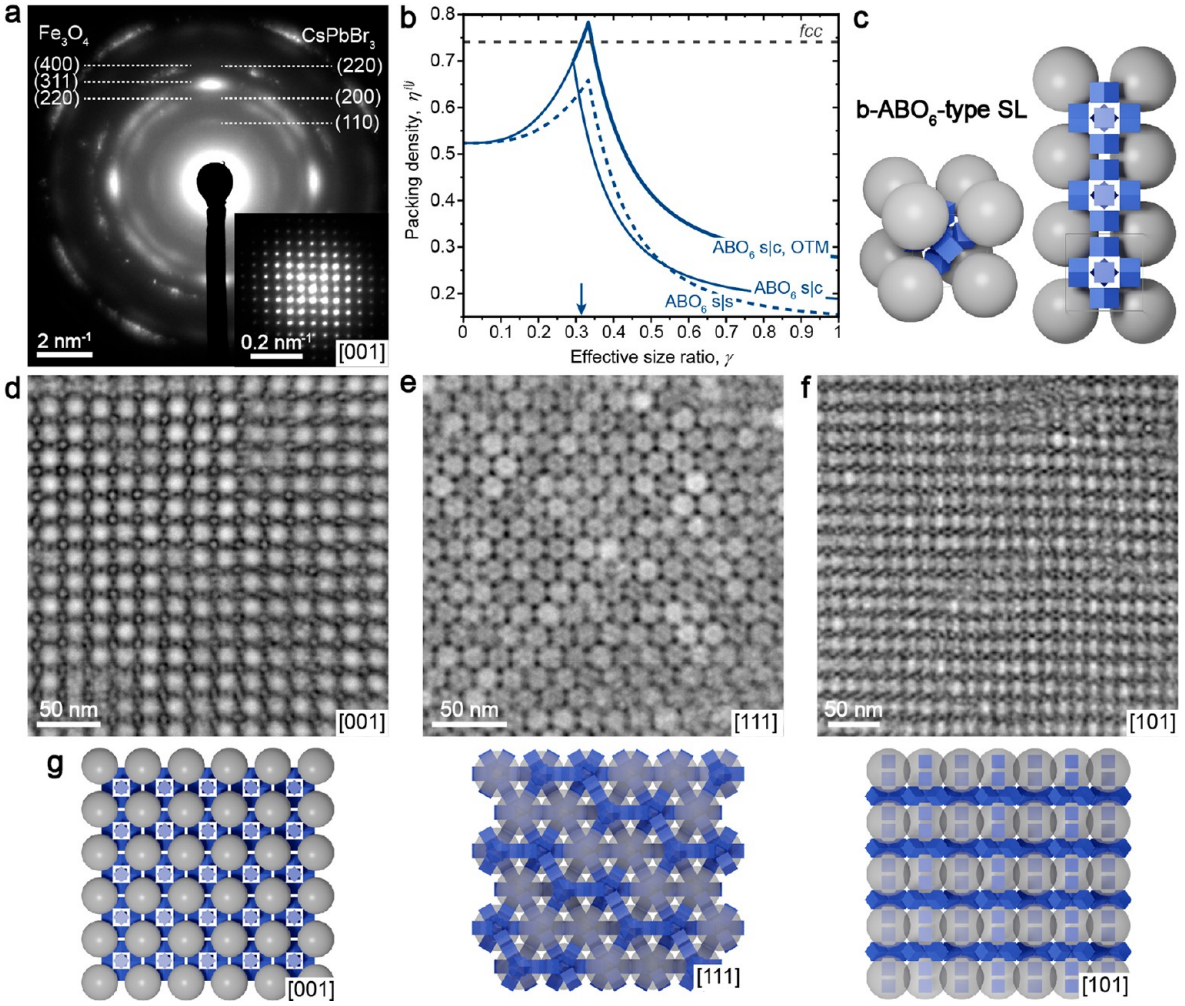

Figure 8. Binary ABO_6-type SLs obtained from 5.3 nm $CsPbBr_3$ and 16.9 nm Fe_3O_4 NCs (γ = 0.315). (a) Wide-angle and (inset) small-angle ED patterns of $[001]_{SL}$-oriented domain. (b) Space-filling analysis for b-ABO_6-type SLs comprising larger spherical and smaller cubic (solid line) or spherical (blue dashed line) NCs within the hard-particle model, except for the indicated OTM branch. (c) Structural model of a b-ABO_6-type unit cell and a slice through $(002)_{SL}$. (d–f) HAADF-STEM images of $[001]_{SL}$-, $[111]_{SL}$-, and $[101]_{SL}$-oriented domains and (g) the corresponding structural models of SL projections.

lattice vectors (Figure 13c). However, the more pronounced (100) peak along the shortest lattice vector may indicate some tilt of the cubes around this direction.

Multicomponent SLs Comprising $FAPbBr_3$ Nanocubes. Apart from cuboid $CsPbBr_3$ NCs, also hybrid organic–inorganic perovskite NCs, namely formamidinium lead bromide ($FAPbBr_3$) NCs can serve as versatile building blocks for NC SLs. For example, 9 nm $FAPbBr_3$ cubes with larger spherical 15.1–19.5 nm $NaGdF_4$ NCs form b-ABO_3-, AlB_2-, and AB_2-type structures (Figure 14a–c). The 5.7 nm $FAPbBr_3$ nanocubes, in analogy to 5.3 nm $CsPbBr_3$ NCs,[58,59] form the NaCl-type SL with 15.1 nm $NaGdF_4$ spheres (Figure 14d) and columnar AB-type or lamellar (which is the dominant product) SLs with 12.5 nm LaF_3 nanodisks (Figure 14e–g).

Self-assembly of Perovskite NCs on Liquid Subphase. Thus, far, the presented SLs were obtained by casting the small volume of the mixture of NCs (ca. 28–35 μL in toluene) over the substrates located in the tilted vial. This simple approach allows for facile screening of the SL formation yet has its drawbacks too. For instance, the range of suitable substrates is rather limited to hydrophobic surfaces. The obtained films usually are characterized by cracks between SL domains that reduce surface coverage. Moreover, adhesion of the SL domain to the substrate, while it still contains solvent, may result in additional crack formation within the domain.[20] Drying-mediated assembly on the surface of an immiscible liquid, usually a polar solvent such as ethylene glycols and acetonitrile, used as support was introduced to overcome these issues, allows for obtaining centimeter-scale SL membranes transferable to the arbitrary substrate, enabling integration of thin-film SLs into devices.[9] This method is, however, difficult to extend to perovskite NCs as even a small but finite solubility in the subphase polar solvent compromises their structural integrity.

After the extensive screening of possible alternatives, we find that glyceryl triacetate is both immiscible with nonpolar solvents such as toluene and hydrocarbons and also does not disperse or chemically harm perovskite NCs and can be utilized as a support in the liquid–air interfacial assembly (see Figure 15a). We also note that fluorinated solvents, such as FC-40, satisfy the aforementioned requirements, but the nonpolar solvents have a low tendency to spread into a needed thin liquid layer on this fluorinated subphase due to

https://doi.org/10.1021/acsnano.1c10702
ACS Nano 2022, 16, 7210–7232

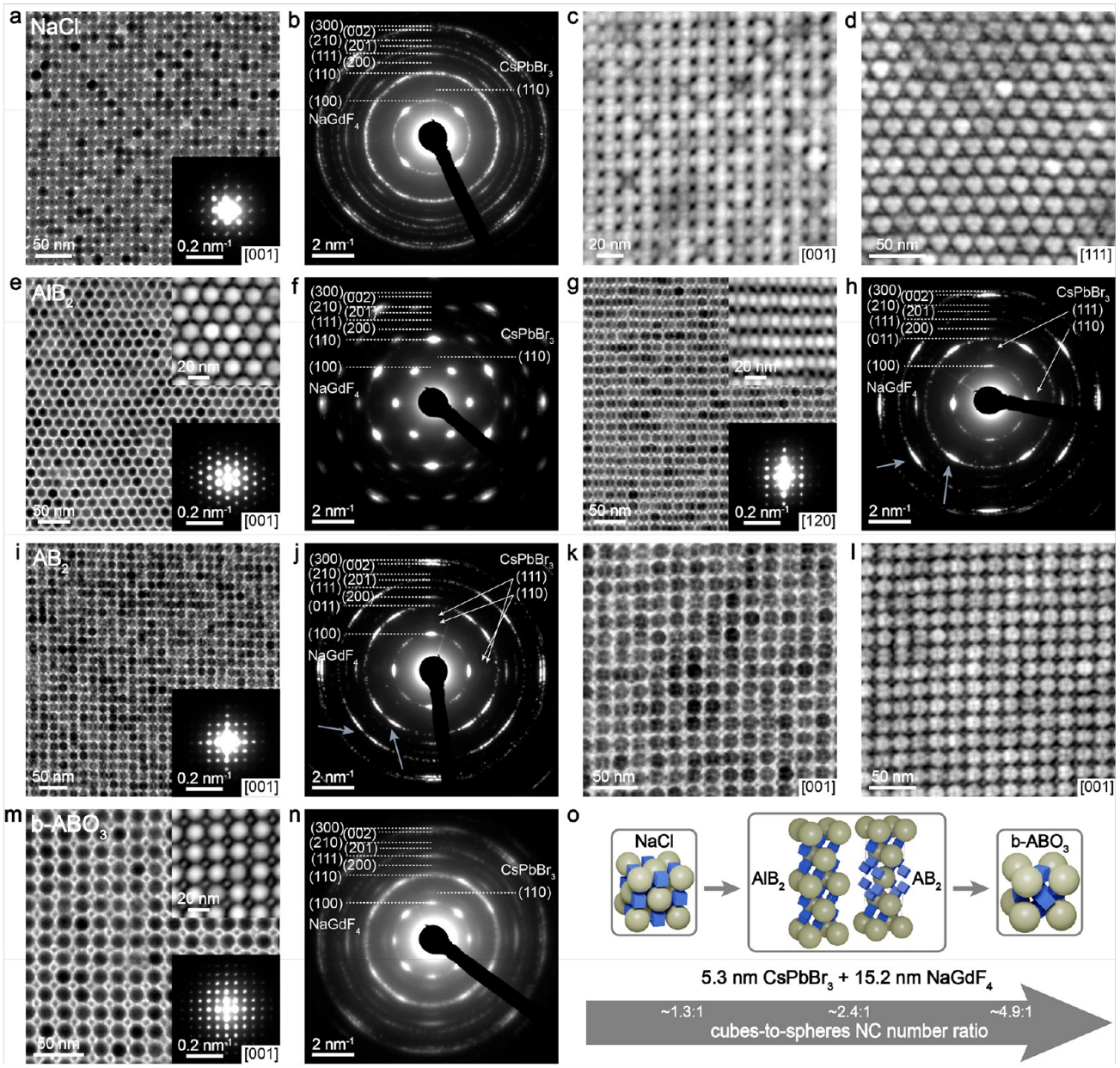

Figure 9. Binary SLs self-assembled from the mixtures of 5.3 nm $CsPbBr_3$ and 15.2 nm $NaGdF_4$ NCs. Increasing the relative concentration of $CsPbBr_3$ NCs changes the experiment outcome from (a–d) NaCl-type to (e–h) AlB_2-type with (i–l) AB_2-type and then to (m, n) ABO_3-type SLs, as illustrated by (o) the scheme. (a, e, i, m) TEM images of $[001]_{SL}$ projections, along with the corresponding (bottom insets) small-angle ED and (b, f, j, n) wide-angle ED patterns; the respective high-magnification HAADF-STEM images are shown as upper insets. (c, d) HAADF images of $[001]_{SL}$- and $[111]_{SL}$-oriented domains. (g) TEM image of $[120]_{SL}$-oriented domain, along with the corresponding (upper inset) HAADF-STEM image, (bottom inset) small-angle ED, and (h) wide-angle ED patterns. (k) Bright-field and (l) HAADF-STEM images of $[001]_{SL}$-oriented domain.

limited wettability. Noteworthy, perfluorodecalin featuring partial miscibility with hexane was successfully used as a substrate for obtaining three-dimensional nearly isotropic perovskite SLs.[54] The self-assembly on glyceryl triacetate occurs within several minutes to several hours depending upon solvent evaporation rate (hexane, octane, decane, or dodecane). Figure 15b–d shows an extended monolayer of $CsPbBr_3$ NCs assembled on the surface of glyceryl triacetate from the solution of NCs in octane. Mixtures of NCs yield ordered binary mono- and multilayers with different structures depending on the concentration, particle number, and size ratios (Figure 15e–g).

Self-Assembly of Binary Supraparticles Comprising Perovskite NCs. Microemulsion-templated self-assembly is another method enabling the control over the superstructure dimensionality and allows for the formation of three-dimensional supraparticles upon the assembly in spherical confinement of the "oil" droplet (colloid) stabilized in an immiscible solvent with the aid of a surfactant.[66,67] Potentially, such ordered multicomponent supraparticles can serve as building blocks for mesoscale materials with hierarchical order, wherein the properties could be defined by constituent NCs, their packing within the supraparticles, and finally by the ordering of supraparticles themselves. Furthermore, dispersed individual

https://doi.org/10.1021/acsnano.1c10702
ACS Nano 2022, 16, 7210–7232

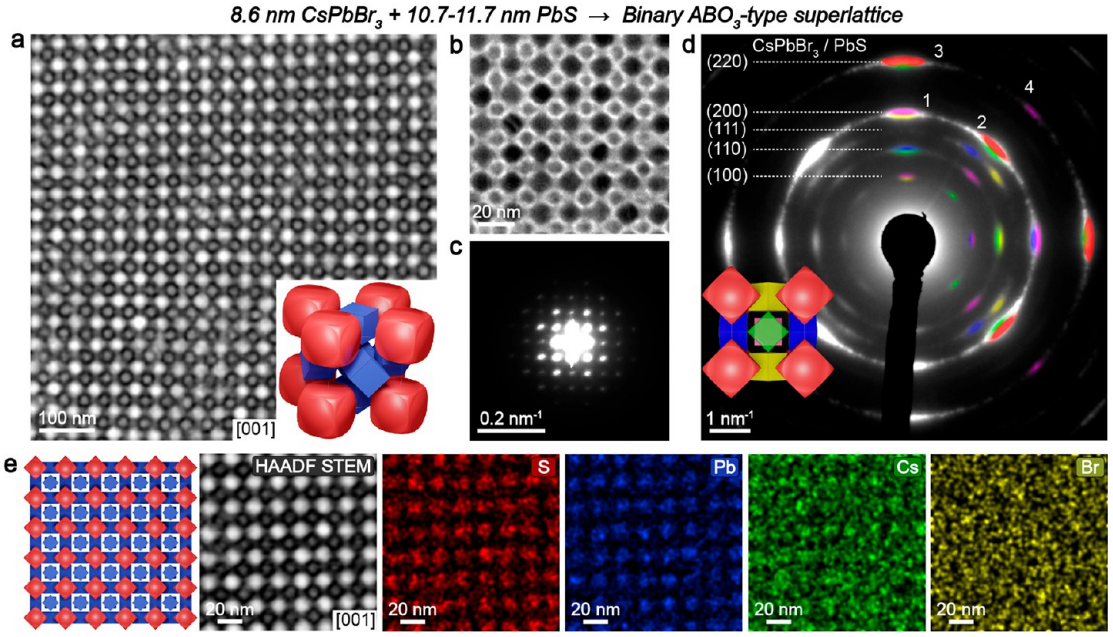

Figure 10. Characterization of b-ABO_3-type SL assembled from 8.6 nm $CsPbBr_3$ and 10.7−11.7 nm PbS. (a) HAADF-STEM image of a single $[001]_{SL}$-oriented binary ABO_3 domain comprising of 8.6 nm $CsPbBr_3$ NCs and 11.7 nm PbS NCs. (b) TEM image of a single b-ABO_3 domain in $[001]_{SL}$ orientation assembled from 8.6 nm $CsPbBr_3$ NCs and 10.7 nm PbS NCs, together with the respective (c) small-angle and (d) wide-angle ED patterns. Diffraction arcs are colored to show their origin from $CsPbBr_3$ and PbS NCs presented as insets. Inset in (a) shows the binary ABO_3 lattice and illustrates the relative position and orientation of NCs. (e) Crystallographic model of a $[001]_{SL}$-oriented ABO_3 lattice, along with HAADF-STEM image and respective EDX-STEM maps for S (red, K-line), Pb (blue, L-line), Cs (green, L-line), and Br (yellow, K-line).

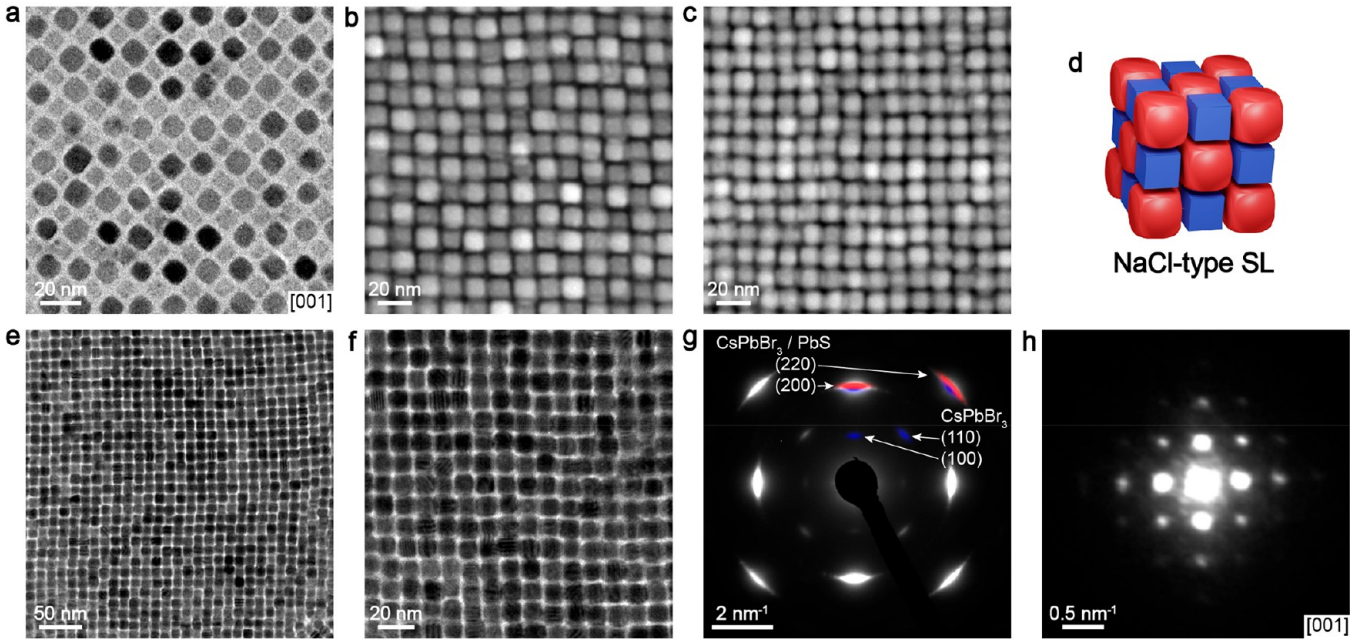

Figure 11. NaCl-type binary SLs from 8.6 nm $CsPbBr_3$ NCs combined with truncated cuboid PbS NCs. (a) TEM image of a monolayer domain. (b, c) HAADF-STEM images of SL domains with an increasing number of layers. (e, f) TEM images of $[001]_{SL}$-oriented SL domains at different magnification, along with the (g) wide-angle and (h) small-angle ED patterns measured from the domain shown in (f); the reflections from $CsPbBr_3$ and PbS NCs are colored to match the NCs in the structural model (d). Images from (a, c, f−h) were obtained with 10.7 nm PbS NCs (γ = 0.778) and from (b, e) with 11.7 nm PbS NCs (γ = 0.720).

supraparticles can be, in principle, manipulated and deposited on-demand into desired locations within photonic and other structures. Colloidal spheres of mono- and binary SLs were reported to form from the emulsions of nonpolar solvents in water.[12,68,69] Recently, a carrier solvent−surfactant pair suitable for dispersing perovskite NC colloidal droplets (in toluene) was developed, namely, fluorinated solvents FC-40 or HFE-750 and fluorinated surfactant 008-FS, yielding single-component perovskite supraparticles.[70] Here, we extend the method to binary SLs with perovskite NCs (Figure 16).

https://doi.org/10.1021/acsnano.1c10702
ACS Nano 2022, 16, 7210−7232

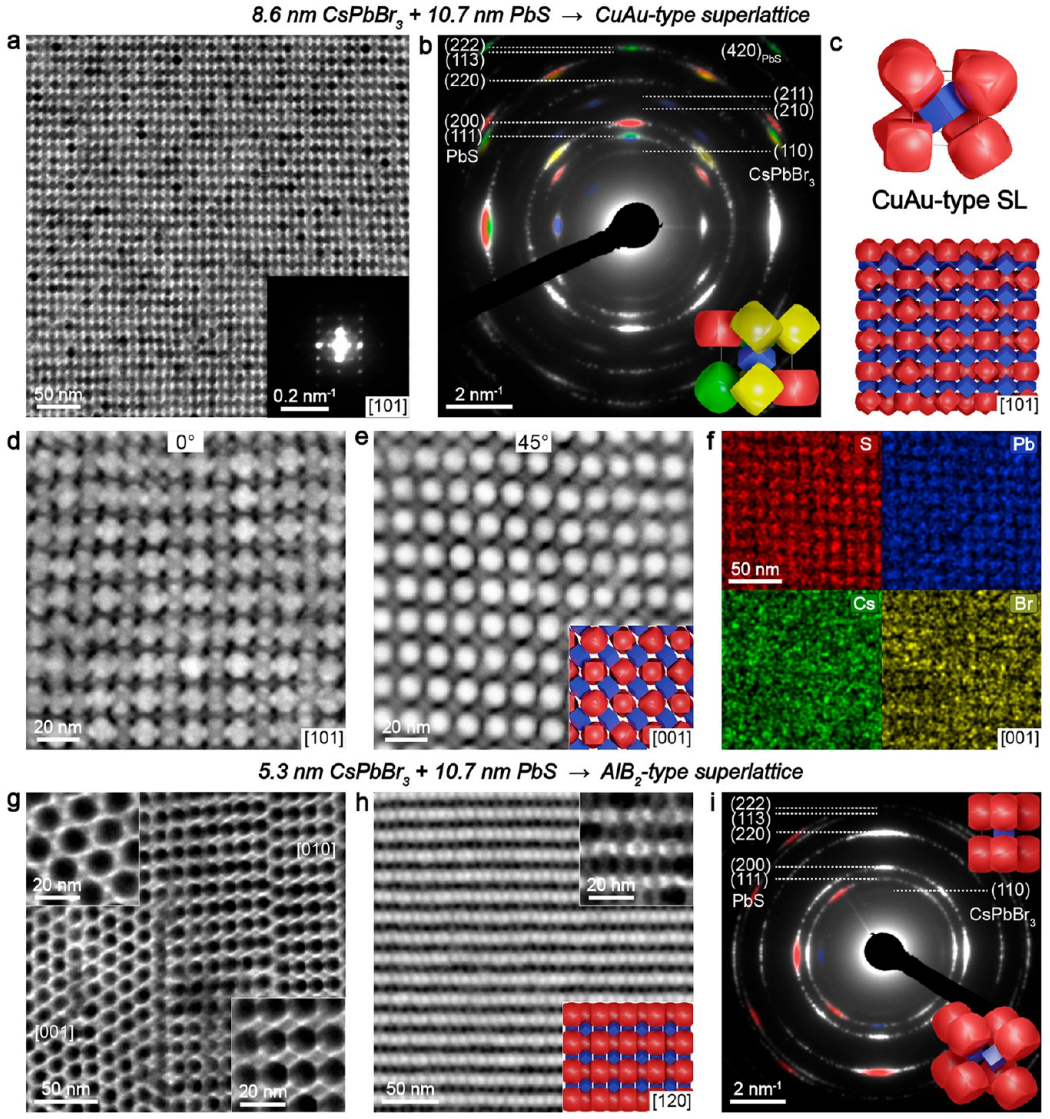

Figure 12. CuAu- and AlB_2-type binary SLs assembled from truncated cuboid 10.7 nm PbS NCs and, respectively, 8.6 and 5.3 nm $CsPbBr_3$ cubes. (a) TEM image of a single CuAu-type SL domain in $[101]_{SL}$ orientation, along with the corresponding (inset) small-angle ED and (b) wide-angle ED patterns (the origin of the reflections is color-coded to match the NCs in the model shown as inset). (c) CuAu unit cell and crystallographic model of $[101]_{SL}$-oriented lattice assuming preferable orientations of NCs in agreement with ED. (d) HAADF-STEM images of a SL domain taken at 0° and 45° tilting angles around $[010]_{SL}$ that correspond to $[101]_{SL}$ and $[001]_{SL}$ orientations, respectively; crystallographic model of $[001]_{SL}$-oriented CuAu-type lattice is depicted in the inset of (e). (f) EDX-STEM elemental maps recorded from a $[001]_{SL}$-oriented domain shown in (e). (g) TEM image of AlB_2-type SL with twist grain boundaries between $[001]_{SL}$- (magnified in upper inset) and $[010]_{SL}$-oriented (magnified in bottom inset) domains. (h) HAADF-STEM, high-magnification TEM image (upper inset), and crystallographic model (bottom inset) along with (i) wide-angle ED pattern of $[120]_{SL}$-oriented AlB_2-type SL. Bottom and upper ($[120]_{SL}$ orientation) insets in (i) represent the unit cell of AlB_2-type SL with orientations of NCs that result in the most intense wide-angle ED spots marked in red (PbS) and blue ($CsPbBr_3$).

Supraparticles with b-ABO_3-type structures can be obtained from the emulsions of 8.6 nm $CsPbBr_3$ and 18.6 nm $NaGdF_4$ NCs (Figure 16b). Smaller domains appear to be single crystalline, albeit, as revealed by electron tomography reconstruction[71] (see Supplementary Video 3), they may possess structural defects such as nanocube vacancies. The growth inside larger droplets leads to 500−1500 nm supraparticles and is characterized by several nucleation sites resulting in polycrystalline SLs[72] (see SEM images in Figure 16b). Perovskite cubes with thick $NaGdF_4$ disks form supraparticles with the ordering analogous to the CaC_2-like structure (Figure 16c) presented earlier (Figure 13).

Collective Optical Properties of b-ABO_3 and AlB_2-type SLs. An exceptional emissivity of lead halide perovskite NCs motivates the exploration of their properties at both single-particle and ensemble levels. Here, we focus on the optical properties where, already on the single-NC level, perovskite NCs are standing out because of their exceptionally fast radiative rates and high oscillator strength[73] and long exciton coherence.[45,74] Scalable self-assembly from colloids makes for an attractive path to the controlled aggregate states of these bright emitters. The relationship between the periodic mesostructure and emerging collective luminescent characteristics can then be delineated and rationalized. Collective PL properties had been observed in our earlier work on

https://doi.org/10.1021/acsnano.1c10702
ACS Nano 2022, 16, 7210−7232

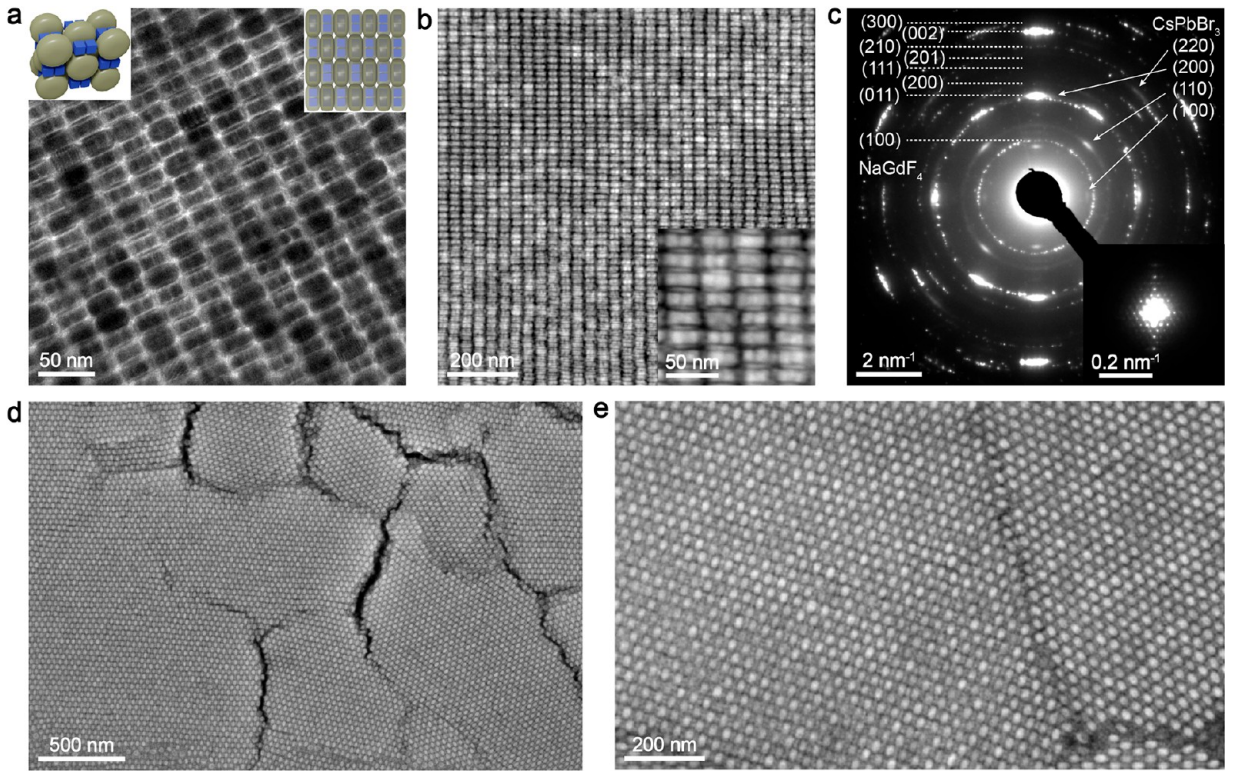

Figure 13. CaC_2-like SL assembled from 8.6 nm $CsPbBr_3$ nanocubes and 31.5 nm $NaGdF_4$ thick nanodisks, featuring sets of two cubes on one lattice site. (a) TEM image and the SL models are shown as insets. (b) HAADF-STEM images at different magnifications, along with the corresponding (c) wide-angle ED and (inset) small-angle ED patterns. (d, e) SEM images at different magnifications.

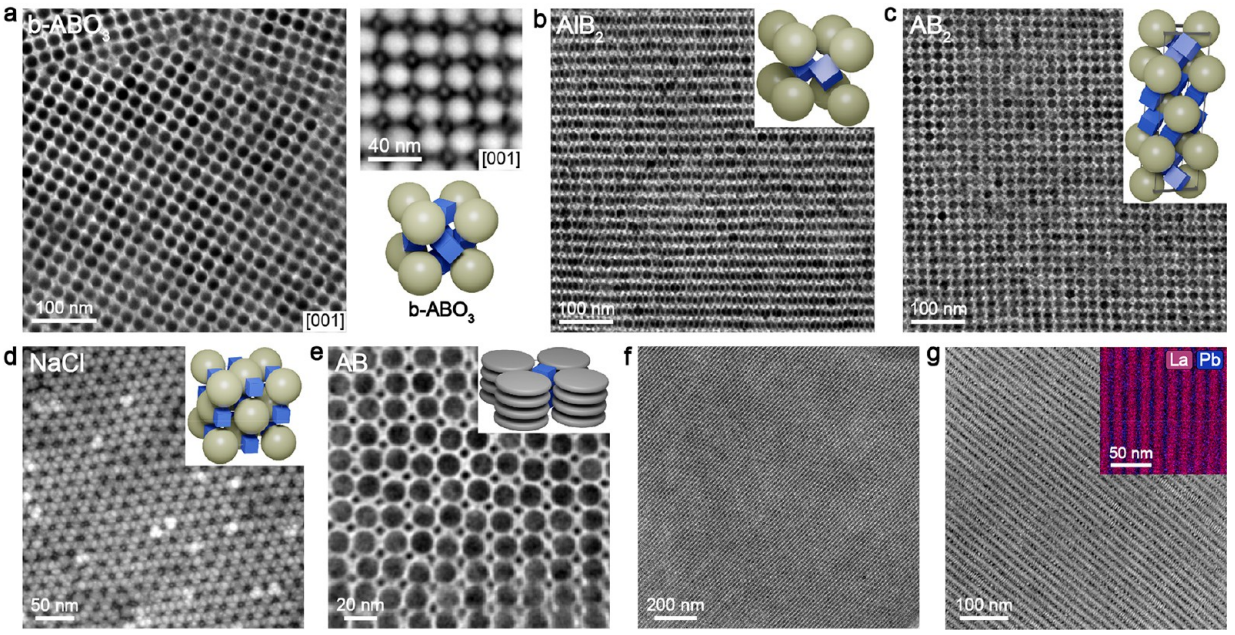

Figure 14. Binary SLs obtained from $FAPbBr_3$ nanocubes. (a) TEM and HAADF-STEM (top right panel) images of a b-ABO_3-type SL assembled from 9 nm $FAPbBr_3$ and 19.5 nm $NaGdF_4$ NCs; SL model is shown in the bottom right panel. (b, c) Bright-field STEM images of, respectively, an [120]-oriented AlB_2-type and $[001]_{SL}$-oriented AB_2-type SL domains comprising 9 nm $FAPbBr_3$ and 15.1 nm $NaGdF_4$ NCs. (d) HAADF-STEM image of an [111]-oriented NaCl-type SL domain comprising 5.7 nm $FAPbBr_3$ and 15.1 nm $NaGdF_4$ NCs. (e) Bright-field STEM image of a columnar AB-type SL domain obtained from 5.7 nm $FAPbBr_3$ NCs and 12.5 nm LaF_3 nanodisks. (f) TEM and (g) HAADF-STEM images of lamellar SL obtained from 5.7 nm $FAPbBr_3$ NCs and 12.5 nm LaF_3 nanodisks; EDX-STEM elemental maps for La (magenta, L-line) and Pb (blue, L-line) are shown in the inset in (g). Insets in (b–d) are SL models.

monocomponent $CsPbBr_3$ NC SLs[53] and binary ABO_3-type SLs ($CsPbBr_3$ cubes + $NaGdF_4$ spheres),[58] studied at cryogenic temperatures. Already with cw-excitation, coupling between perovskite NCs is apparent from the sharp PL band,

https://doi.org/10.1021/acsnano.1c10702
ACS Nano 2022, 16, 7210−7232

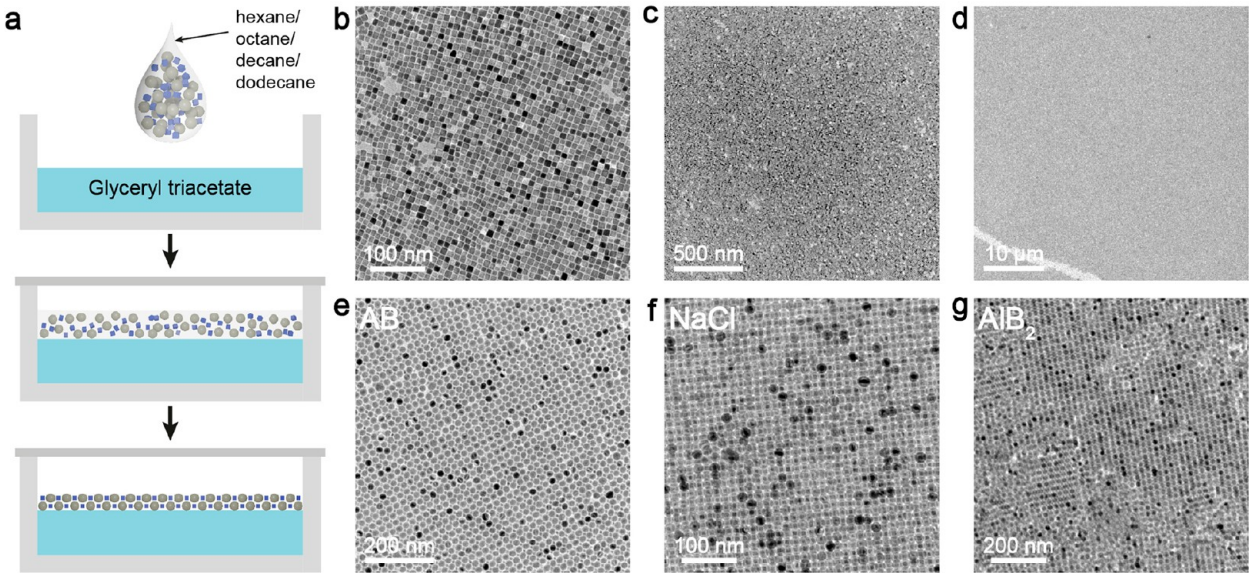

Figure 15. Self-assembly of perovskite NCs at the liquid−air interface. (a) Illustration of the assembly process: NCs dispersed in nonpolar solvents are cast onto the surface of glyceryl triacetate in a Teflon well or Petri dish, which is then covered with glass or larger Petri dish, respectively; ordered SL film floating on the subphase is formed upon evaporation the solvent. (b−d) TEM images of 9 nm $CsPbBr_3$ NC monolayer obtained from octane on glyceryl triacetate. (e−g) TEM images of AB-type monolayer (obtained from dodecane) and NaCl- and AlB_2-type films (obtained from decane), respectively, comprising 8.6 nm $CsPbBr_3$ and 19.8 nm Fe_3O_4 NCs.

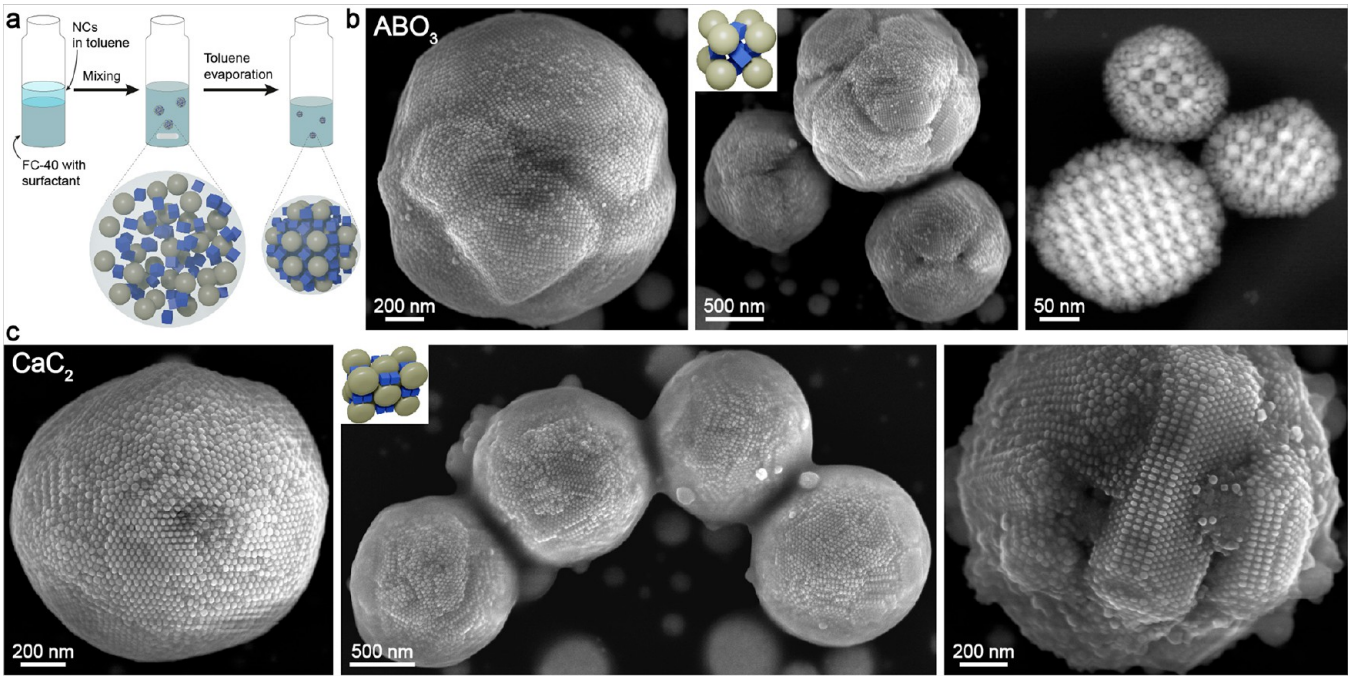

Figure 16. Oil-in-oil templated assembly of binary SLs comprising perovskite NCs. (a) Illustration of the assembly process: NCs dispersed in toluene are mixed with a fluorinated solvent (FC-40) containing surfactant (008-FS) that is capable of stabilizing droplets with NCs. Slow evaporation of toluene from the droplets during stirring results in the formation of ordered binary supraparticles. (b) SEM and HAADF-STEM (right panel) images of supraparticles with b-ABO_3 structure obtained from 8.6 nm $CsPbBr_3$ cubic and 18.6 nm $NaGdF_4$ spherical NCs. (c) SEM images of supraparticles with CaC_2-like structure assembled from 8.6 nm $CsPbBr_3$ nanocubes and 31.5 nm $NaGdF_4$ thick nanodisks. Insets in (b, c) show the SL models.

red-shifted with respect to the excitonic PL of uncoupled NCs. Furthermore, for the same samples, pulsed excitation with higher fluencies gives rise to superradiant emission, specifically superfluorescence. Superfluorescence emerges when coherence is established over a number of excited emitters via a common radiation field, forming a giant dipole. This then manifests itself as short (subnanosecond) and intense (proportional to the squared number of coupled emitters) bursts of light.

Herein, we survey the behavior of the red-shifted PL band, as well as concomitant absorption band, from the coupled NCs in relation to the lattice structure and NC size and composition. Such energetically shifted emission and absorption bands are well-known for molecular aggregates, where the

https://doi.org/10.1021/acsnano.1c10702
ACS Nano 2022, 16, 7210−7232

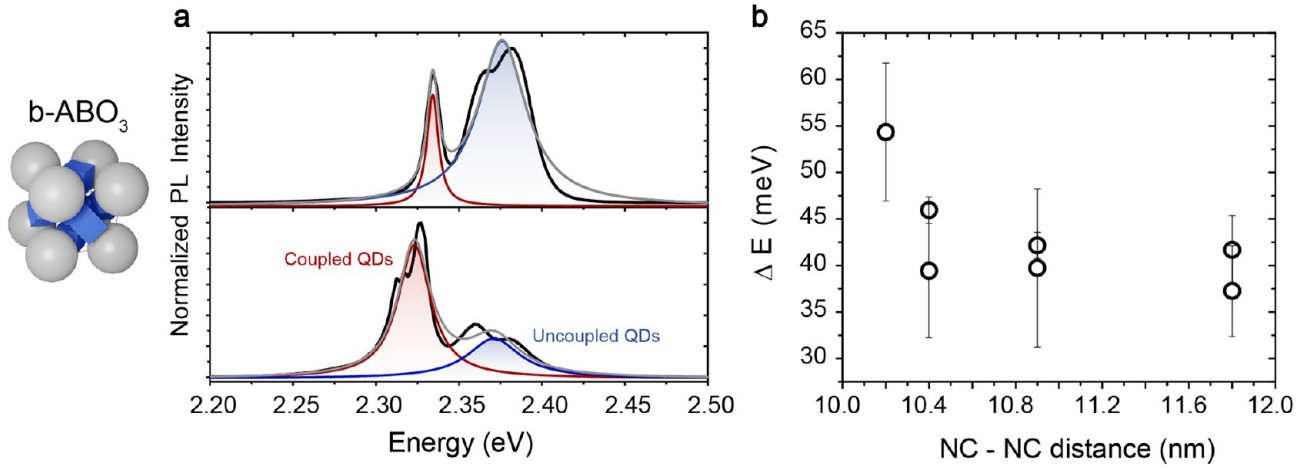

Figure 17. PL properties of ABO_3-type binary SLs at 6 K. (a) PL spectra of binary ABO_3-type SLs assembled by employing 8.6 nm $CsPbBr_3$ and 19.5 nm (top) or 14.5 nm (bottom) Fe_3O_4 NCs. The PL spectra (black solid lines) are fitted to a doubled Lorentzian function (red and blue lines are the individual functions, while the gray lines are the cumulative fits to the experimental data). (b) Measured coupled vs uncoupled splitting energy for several samples with different distances between O-site and B-site NCs. Error bars denote the standard deviation obtained by measuring several PL spectra on different locations on the same sample.

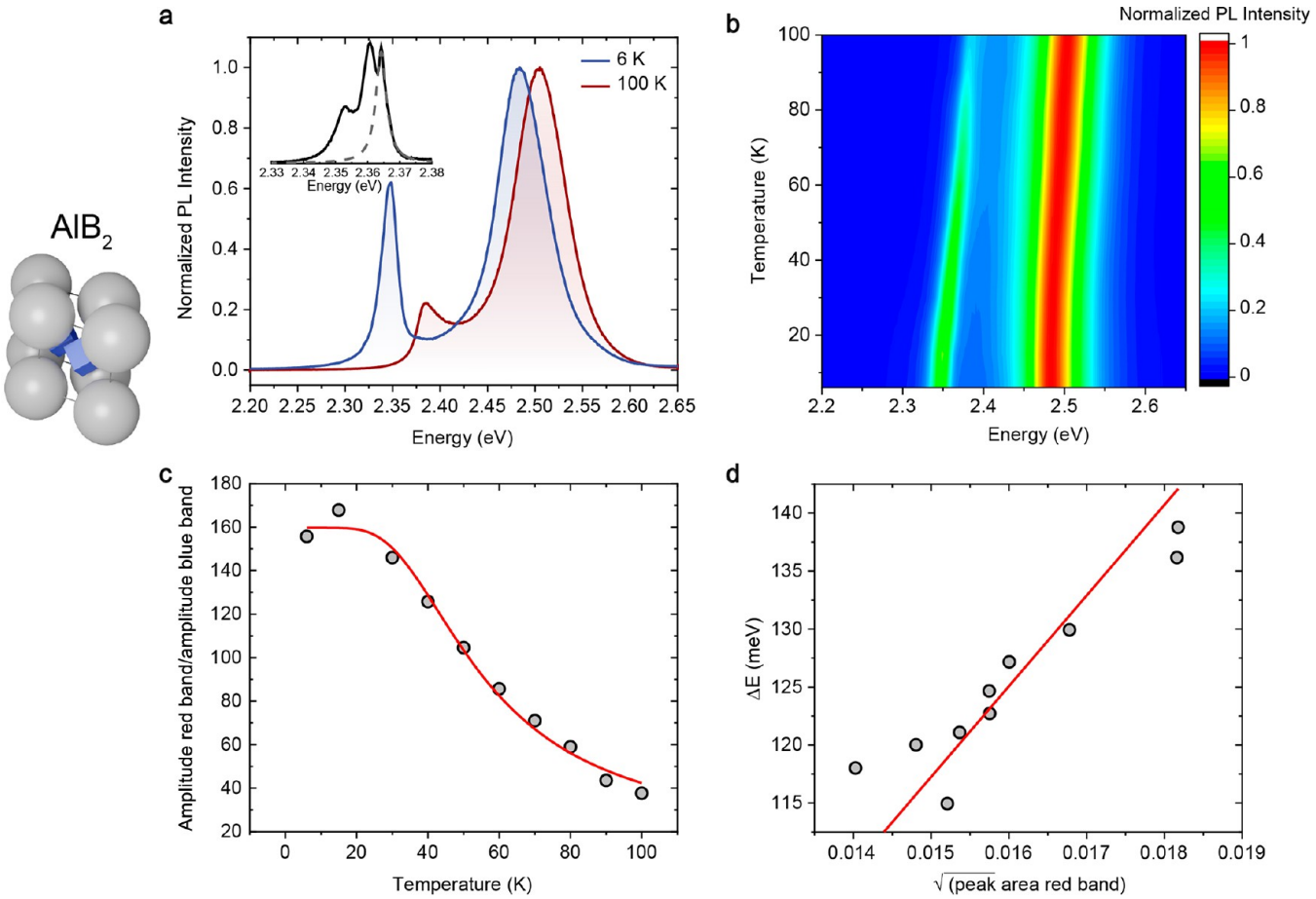

Figure 18. Impact of the temperature on the PL band from coupled NCs in AlB_2-type binary SLs (5.3 nm $CsPbBr_3$ NCs + 12.5 nm Fe_3O_4 NCs). (a) Normalized PL spectra for the AlB_2-type SLs at 6 and 100 K. The inset reports a zoom-in PL spectrum for a nominally similar sample where much narrower emission peaks are resolved (full width at half-maximum of about 3 meV, dashed line). (b) Two-dimensional colored plot of normalized PL spectra obtained at different temperatures. (c) The relative amplitude of the two emission bands as a function of temperature (black open circles). The red solid line is the best fit to an Arrhenius plot returning activation energy of 14 meV, very close to the LO-phonon energy of $CsPbBr_3$ crystal (17 meV). (d) Extracted splitting energy is plotted vs the squared root of the red-shifted peak area, exhibiting a linear dependence (solid red line).

https://doi.org/10.1021/acsnano.1c10702
ACS Nano 2022, 16, 7210−7232

coherent coupling in J-/H-aggregates can lead to super/subradiant emission.[75] Hence, we interpret the emergence of this additional emission band next to the excitonic PL band as emission that originates from coupled NC that is induced by the NC assembly into ordered SLs. The energy splitting between these bands may be viewed as a signature of the coupling strength. In Figure 17a, we show the emission spectra of two b-ABO_3 SLs with 8.6 nm $CsPbBr_3$ nanocubes and iron oxide NCs of different sizes. As the A-sphere (Fe_3O_4) size increases from 14.5 to 19.5 nm, so does also the lattice parameter and hence the B−O sites distance (from 10.2 to 11.8 nm), as seen experimentally by TEM and GISAXS. The PL peak energy splitting between uncoupled NCs and the coupled NCs decreases from 54 ± 7 meV to 37 ± 5 meV (Figure 17a). In b-ABO_3-type SLs, NCs are in very close proximity (the distance between inorganic cores of perovskite NCs is below 1.4 nm), potentially allowing a wave function tunneling. Contrary to the long-range dipole−dipole coupling, which exhibits a characteristic $1/D^6$ scaling of the coupling strength as a function of the distance D between the dipoles, Dexter-like wave function tunneling is expected to exhibit exponential behavior. The exact determination of the underlying physical mechanism responsible for the NC coupling remains to be further explored; in particular, whether B−O or O−O sites couple by the short-range wave function overlap or whether there exists longer-range B−B (a unit cell apart) dipolar coupling or similar.

In molecular aggregates, the coupling between the constituent molecules and, therefore, the aggregate emission band can exhibit peculiar temperature trends.[75] In order to shed light on the role of such phonon-related processes within the NC aggregates, temperature-dependent measurements were carried out on AlB_2 SLs formed by 5.3 nm $CsPbBr_3$ NCs and 12.5 nm iron oxide NCs. We chose this SL structure given the large energetic splitting (ca. 140 meV) observed for this SL type. Although the geometry of the perovskite NC sublattice and crystallographic alignment of NCs is vastly different than in b-ABO_3 SLs, thus precluding a trustful comparison, the enhanced red-shift could be assigned to the shorter NC−NC distance (ca. 9.5 nm) and higher quantum confinement obtained with 5.3 nm $CsPbBr_3$ NCs. Figure 18a shows typical PL spectra at low (6 K) and elevated (100 K) temperatures, whereas complete temperature evolution is shown in Figure 18b. While the emission band of the uncoupled NCs (near 2.50 eV) shifts only slightly to blue, the emission from the coupled NCs shifts more, reducing the energetic splitting and decreasing in relative intensity while broadening. Spectral substructure of the coupled PL band is occasionally seen (inset of Figure 18a), which we attribute to several distinct aggregate domains being present within the excitation beam spot of ca. 2 μm^2. We note that while a large fraction of studied SLs display the red-shifted emission from coupled NCs, its appearance still varies from sample to sample, probably due to the very short-range nature of the coupling, being it either wave function tunneling or partial necking of the NCs.

The ratio between the coupled (aggregate) and the uncoupled (nonaggregate) NC emission is plotted in Figure 18c, along with an Arrhenius fit, returning activation energy of about 14 meV, close to the LO-phonon energy in $CsPbBr_3$ NCs (17 meV).[76,77] This suggests that a phonon-driven mechanism similar to that in molecular aggregates reduces the effective number of coupled emitters N with temperature rise. This notion is supported by rather linear correlation obtained when plotting the splitting ΔE between the coupled and the uncoupled emission bands vs the square root of the peak area of the coupled emission (using the temperature-dependent data), which represents the number of coupled emitters ($\Delta E \propto \sqrt{N}$, Figure 18d). This dependency and the emission of coupled NCs being far from the expected bulk emission (ca. 2.3 eV, 535−540 nm) as well as a very strong quenching of the red aggregate band already at intermediate temperatures would hardly be reconcilable with an alternative assumption that the red-shifted emission peak could originate from the bulk material forming during the aggregation process.[78] The latter would imply an order of magnitude reduction of bulk emission quantum yield just within this temperature range.

Further evidence for red-shifted PL band originating from coupled NCs is found in the absorption spectra, presented here for b-ABO_3-type SLs (8.8 nm $CsPbBr_3$ + $NaGdF_4$ NCs, Figure 19). These SLs exhibit two emission bands with a relative

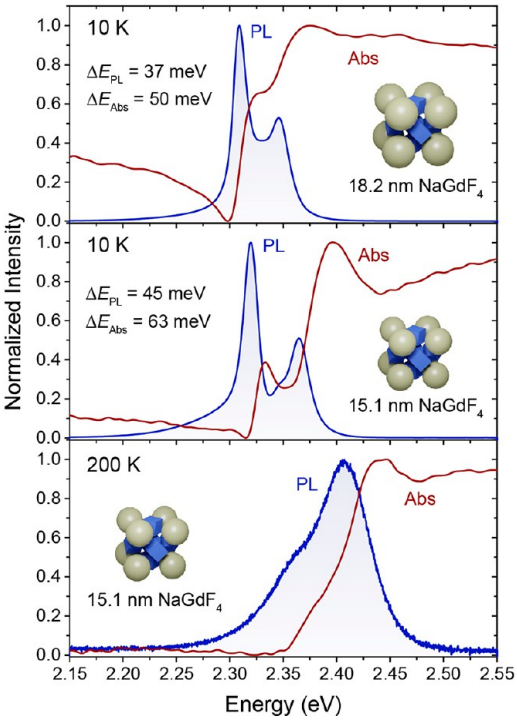

Figure 19. PL and absorbance spectra of binary ABO_3-type SLs comprising 8.8 nm $CsPbBr_3$ cubes and 18.2 nm (top panel) or 15.1 nm (middle panel) $NaGdF_4$ spherical NCs, measured at 10 K (top and middle panel) and 200 K (bottom panel).

energetic splitting (ΔE) scaling with the NC-to-NC distances: on average, 45 and 37 meV for 15.1 and 18.2 nm $NaGdF_4$ NCs, respectively (Figure 19, top and middle panels). The red-shifted band is also resolved in absorption, similar to our earlier studies on single-component SLs.[53] Similar to the PL behavior, the relative energetic splitting scales with the lattice parameter of the SL. The temperature behavior is analogous too; an additional absorption band vanishes when reaching 200 K (Figure 19), being strong evidence that rules out the hypothesis attributing the red-shifted PL band to bulk inclusions.[78] In particular, while a drop of the PL intensity from the bulk inclusions upon heating could be rationalized by the rapidly decaying PL quantum yield, the absorbance must persist.

https://doi.org/10.1021/acsnano.1c10702
ACS Nano 2022, 16, 7210−7232

CONCLUSIONS

In summary, we have presented a full survey of multicomponent SLs comprising sharp, sub-10 nm cubic perovskite NCs, obtained thus far in our experiments by combining them with spherical, truncated cubic, and disk-shaped NCs. Three SL structure types are of the kind commonly reported for binary mixtures of spherical NCs (NaCl, AlB_2, and CuAu types). Three other binary structures (perovskite ABO_3, AB_2, ABO_6) are related to the cubic shape of perovskite NC building blocks. AB_2 can be viewed as derived from AlB_2 by slipping each fourth $(100)_{SL}$ in an $[011]_{SL}$ direction. ABO_6 can be conceived as the ABO_3 lattice, wherein each O-site is occupied by two 5.3 nm $CsPbBr_3$ cubes. When an anisotropic NC counter building block is utilized, namely, thick $NaGdF_4$ nanodisks (18.5 nm thick, 31.5 nm in diameter), a CaC_2-like lattice forms, wherein the 8.6 nm cubes occupy the "C_2-site", and the anisotropy of disks reduces tetragonal symmetry of the unit cell into orthogonal. In all studied SLs, cubic NCs are orientationally locked. We also report a substrate-less growth of thin-film SLs by drying colloids atop of an immiscible liquid (glyceryl triacetate) or of SL supraparticles with the aid of emulsion. Low-temperature PL and absorption spectra attest emergence of collective states in these highly dense aggregates of highly luminescent NCs.

EXPERIMENTAL SECTION

Synthesis of Cesium Oleate Stock Solution. Cs_2CO_3 (0.2 g, Sigma-Aldrich, 99.9%), oleic acid (0.6 mL, OA, Sigma-Aldrich, 90%, vacuum-dried at 100 °C), and 1-octadecene (7.5 mL, ODE, Sigma-Aldrich, 90%, distilled) were loaded into 25 mL flask, dried under vacuum for 20 min at 100 °C, and then heated under N_2 to 120 °C until all the Cs_2CO_3 reacted with OA.

Synthesis of $CsPbBr_3$ NCs. The 8.6 nm NCs were synthesized following the method reported in ref 62. In a 25 mL three-neck flask, $PbBr_2$ (55 mg, ABCR, 98%) was degassed three times, suspended in 5 mL of ODE, and degassed three times again at room temperature. The suspension was quickly heated to 180 °C, when the temperature reached 120 °C, 0.5 mL of OA and oleylamine (0.5 mL, OLA, Strem, 97%, distilled) were injected. At 180 °C, preheated to about 100 °C cesium oleate solution in ODE (0.6 mL) was injected. The reaction mixture was cooled immediately to room temperature with an ice bath. The crude solution was centrifuged at 12,100 rpm (equivalent to 20,130 relative centrifugal force) for 5 min, the supernatant was discarded, and the precipitate was dispersed in hexane (0.3 mL, Sigma-Aldrich, anhydrous, 95%). The solution was centrifuged again at 10,000 rpm for 3 min, and the precipitate was discarded. Then, OLA/OA ligands were exchanged by DDAB treatment. 0.3 mL hexane, toluene (0.6 mL, Sigma-Aldrich, anhydrous, 99.8%), and DDAB (0.14 mL, 0.05 M in toluene, Sigma-Aldrich, 98%) were added to the supernatant and stirred for 1 h, followed by destabilization with ethyl acetate (1.8 mL, Sigma-Aldrich, 99.9%), centrifuging at 12,100 rpm for 3 min and redispersing in 0.6 mL of toluene. Synthesis of 5.3 nm $CsPbBr_3$ NCs was adopted from ref 61 followed by DDAB treatment. The concentration of $CsPbBr_3$ NCs was calculated from the optical absorption at 335 nm using the reported molar extinction coefficient.[79] The concentration of other NCs was determined gravimetrically, accounting for capping ligands with the grafting densities stated in Supplementary Note 2.

Synthesis of $NaGdF_4$ NCs by Thermal Decomposition of Gadolinium Trifluoroacetate.[31] Gadolinium trifluoroacetate (147 mg, 0.267 mmol), NaF (16.1−22.4 mg, 0.383−0.533 mmol, lower loading resulted in larger NCs size, Merk, 99.99%), 4 mL of OA, and 4 mL of ODE were degassed in a three-neck flask at 125 °C for 70 min. Then the solution was heated to 312 °C at 15 °C/min under nitrogen and kept at this temperature for 75 min. The reaction mixture was cooled to room temperature, and 36 mL of ethanol (Merck, 99.8%) was added to destabilize the colloidal solution. The NCs were precipitated by centrifugation at 4000 rpm for 3 min and washed three additional times with hexane (along with 25 μL OA) and ethanol (1 to 1.5 by volume). After purification, NCs were stored in 2 mL of hexane. Gadolinium trifluoroacetate was synthesized by reaction of Gd_2O_3 (2.159 g, 6 mmol, Sigma-Aldrich, 99.9%) with trifluoroacetic acid (7.4 mL, 95 mmol, Sigma-Aldrich, 99%) and 12.4 mL of water under reflux (93 °C) for 1 h. The white product was isolated by evaporation of the unreacted acid and water under vacuum at 60 °C and dried overnight under vacuum.

For the synthesis of $NaGdF_4$ disks, gadolinium trifluoroacetate (221 mg, 0.4 mmol), NaF (29.5 mg, 0.7 mmol), 6 mL of OA, and 6 mL of ODE were degassed in a three-neck flask at 125 °C for 90 min. Then the solution was heated to 312 °C at 15 °C/min under nitrogen and kept at this temperature for 83 min. The reaction mixture was cooled to room temperature, then 2 mL of hexane and 36 mL of ethanol were added to destabilize the colloidal solution. The NCs were precipitated by centrifugation at 5000 rpm for 2 min and washed additionally twice with hexane (along with 40 μL of OA) and ethanol (1:2.5 by volume). After purification, NCs were stored in 2 mL of toluene.

Synthesis of Truncated Cubic PbS NCs.[80] For a synthesis of 10.7 nm PbS NCs, PbO (278.8 mg, 1.25 mmol, Aldrich, 99%), OA (3.125 mL, 9.88 mmol), and 6.25 mL of ODE were degassed in a three-neck flask for 30 min at room temperature and 30 min at 100 °C. Then the solution was flushed with nitrogen and heated to 200 °C. At this temperature, sulfur (40 mg, 1.25 mmol, Fluka, 99.5%) dissolved in OLA (1.25 mL 3.8 mmol) was swiftly injected. The reaction mixture was cooled to room temperature with a water bath after 5 min of stirring. The NCs were washed four times with hexane (along with 25 μL OA) and ethanol (3:1 by volume) and stored in hexane. For the synthesis of 11.7 nm PbS NCs, the mixture of 2.2 mL of OA with 7.2 mL of ODE was used as a solvent, and the reaction temperature was increased to 205 °C.

Synthesis of Fe_3O_4 NCs by Thermal Decomposition of Iron Oleate.[63] For the synthesis of iron oleate complex, $FeCl_3$ (1.658 g, 10 mmol, Alfa-Aesar, 98%) and sodium oleate (9.125 g, 30 mmol, TCI, 97%) were dissolved in a mixture of 35 mL of hexane, 20 mL of ethanol, and 15 mL of distilled water. After stirring under nitrogen at 65 °C for 5 h, the upper organic layer was separated and washed five times with warm water, followed by centrifugation and isolation in a separatory funnel. The waxy solid product was isolated using a rotary evaporator and dissolved in ODE to form 0.4 mol/kg solution. In a typical synthesis of 15.6 nm Fe_3O_4 NCs, iron oleate complex in ODE (5 mL), OA (0.8 mL, 2.53 mmol), and 5 mL of ODE were loaded into a three-neck flask and vacuum dried at 110 °C for 90 min. The reaction mixture was then heated under nitrogen from 200 to 312 °C with a constant heating rate of 2 °C/min and maintained at this temperature for 30 min after the initiation took place. The solution was cooled to room temperature and washed with 3 mL of hexane and 12 mL of acetone, followed by centrifugation at 8000 rpm for 3 min. The precipitate was dissolved in 3 mL of hexane with 25 μL of OA. After two additional rounds of purification with hexane and acetone (2:1 by volume), the NCs were dispersed in 3 mL hexane. The size of NCs was controlled by varying the concentration of OA (higher for larger NCs) and reaction temperature (higher for larger NCs).

Synthesis of 12.5 nm LaF_3 Nanodisks by Thermal Decomposition of Lanthanum Trifluoroacetate.[37] Lanthanum trifluoroacetate (192 mg), LiF (31.2 mg, Sigma-Aldrich, 99.99%), 6 mL of OA, and 6 mL of ODE were degassed in a 25 mL three-neck flask at 125 °C for 2 h. Then the solution was heated to 300 °C at 15 °C/min under nitrogen and kept at this temperature for 70 min. The reaction mixture was cooled to room temperature, and 3 mL of hexane along with ethanol (30 mL) was added to destabilize the colloidal solution. The NCs were precipitated by centrifugation at 4000 rpm for 2 min and washed two additional times with hexane (along with 10−30 μL of OA) and ethanol (1:1 by volume). After purification, NCs were dispersed in 3 mL of hexane, and residual LiF, which is not soluble in nonpolar solvents, was separated by centrifugation at 4000 rpm for 2 min. Lanthanum trifluoroacetate was synthesized by reaction of La_2O_3 (3.24 g, Sigma-Aldrich,

https://doi.org/10.1021/acsnano.1c10702
ACS Nano 2022, 16, 7210−7232

99.999%) with trifluoroacetic acid (16 mL) and 16 mL of water under reflux (93 °C) for 1 h. The white product was isolated by evaporation of the unreacted acid and water under vacuum at 60 °C and dried overnight under vacuum.

Preparation of Multicomponent SLs. Self-assembly of NCs was carried out using a drying-mediated method on carbon-coated TEM grids (carbon type B, Ted Pella, Formvar protective layer was removed by immersing the grid in toluene for 10 s), HF-treated silicon, and silicon nitride TEM windows (Agar Scientific, Norcada). A mixture of NCs in anhydrous toluene had an overall particle concentration of 0.5−2 μM and NC number ratios in the range of 0.5−20. 28−35 μL of NC mixture was transferred into a tilted 2 mL glass vial with a substrate inside. The solvent was evaporated under 0.5 atm pressure at room temperature. For example, binary ABO_3-, AlB_2-, and NaCl-type SLs were obtained with high yields on TEM grids upon slow drying of the solutions prepared by mixing 15.2 nm $NaGdF_4$ NCs (29 mg/mL, 1.8, 2.0, and 2.4 μL, respectively) and 5.3 nm $CsPbBr_3$ NCs (7.5 μM; 4.7, 2.6, and 1.7 μL, respectively) with anhydrous toluene (25 μL); binary ABO_3-type SL, 11.7 nm PbS NCs (1.8 μM, 3 μL), 8.6 nm $CsPbBr_3$ NCs (5.0 μM, 7 μL) and 25 μL of toluene; binary NaCl-type SL, 11.7 nm PbS NCs (1.8 μM, 2.8 μL), 8.6 nm $CsPbBr_3$ NCs (3.9 μM, 3 μL) and 25 μL of toluene.

For the assembly of single-component $CsPbBr_3$ NCs film at the liquid−air interface, a 1 × 1 cm^2 Teflon well was filled with 0.5 mL of glyceryl triacetate (Sigma-Aldrich, 99%), $CsPbBr_3$ NCs in octane (0.4 μM, 20 μL) were dropped onto the surface, and then the well was covered by glass slide and octane slowly evaporated. After drying was completed, the film was transferred to a carbon-coated TEM grid, and the substrate was further dried under vacuum to get rid of the residual subphase. For the assembly of NaCl-type film, the mixture of 8.6 nm $CsPbBr_3$ NCs (4.3 μM, 2.5 μL, in toluene), 19.5 nm Fe_3O_4 NCs (39 mg/mL, 2.5 μL, in toluene), and 10 μL of decane was dropped onto the surface of glyceryl triacetate in Teflon well following the aforementioned procedure. For the assembly of the AlB_2-type film, the mixture of 8.6 nm $CsPbBr_3$ NCs (4.3 μM, 9 μL, in toluene), 19.5 nm Fe_3O_4 NCs (39 mg/mL, 6 μL, in toluene), and 100 μL of decane was dropped onto the surface of glyceryl triacetate (1.5 mL) in Petri dish (3 cm in diameter), covered by glass slide following the aforementioned procedure.

For the typical microemulsion-templated self-assembly, solution 1 ($CsPbBr_3$ and $NaGdF_4$ NCs in toluene with the total NCs concentration about 5 mg/mL) was added into solution 2 (fluorosurfactant 008-FS in fluorinated solvent FC-40). Then, the resulting suspension was mixed with a vortex mixer or a homogenizer. Emulsified solution was slowly stirred for 24−48 h until the toluene was evaporated. For the assembly of a b-ABO_3-type micelle, the mixture of 8.6 nm $CsPbBr_3$ NCs (1.7 μM, 25 μL, in toluene), 18.6 nm $NaGdF_4$ NCs (9 mg/mL, 82 μL, in toluene), and 60 μL of toluene was added to the solution of 5 wt % 008-FS in FC-40 (50 μL, RAN Biotechnologies) and FC-40 (283 μL, abcr) following the aforementioned procedure. For the assembly of an orthorhombic CaC_2-like micelle, the mixture of 8.6 nm $CsPbBr_3$ NCs (1.3 μM, 45 μL, in toluene), 31.5 nm $NaGdF_4$ NCs (2 mg/mL, 90 μL, in toluene), and 32 μL of toluene was added to the solution of 5 wt % 008-FS in FC-40 (50 μL) and FC-40 (283 μL) following the aforementioned procedure.

Electron Microscopy Characterization. TEM and HAADF-STEM images as well as ED and small-angle ED patterns were collected with the use of JEOL JEM2200FS microscope operating at 200 kV accelerating voltage. EDX-STEM maps and HAADF-STEM images at different tilt angles were recorded using an FEI Titan Themis microscope operated at 300 kV equipped with a SuperEDX detector, with the aid of a motorized dual-axis tomography holder. Captured TEM and electron diffraction images were compared with the ones simulated in Crystal Maker 10.4.5 and Single Crystal 3.1.5 software, purchased from CrystalMaker Software Ltd. Electron tomography was carried out in HAADF-STEM mode at 300 kV using a small beam semiconvergence angle of 2.5 mrad, to increase the depth of field. Images were recorded over a tilt angle range ± (57−72)° and interval 2−3°. Reconstruction was done using IMOD with a Back Projection algorithm and SIRT-like radial filter.[81] The tomograms were recorded on SLs self-assembled on carbon-coated TEM grids as continuous films or via a microemulsion technique. SEM images were obtained on a FEI Helios 660 operated at 3−7 kV using immersion mode.

Atomic Force Microscopy. ScanAsyst-AiIR probes were used to analyze the topography of the SLs on the Bruker Icon 3 atomic force microscope.

GISAXS Characterization. GISAXS measurements were performed at the Austrian SAXS beamline of the electron storage ring ELETTRA using a photon energy of 8 keV.[82] The beamline setup was adjusted to a sample to detector distance of 1961.43 mm to result in an accessible horizontal scattering vector q-range of $-1.2\ nm^{-1} < q_H < 1.8\ nm^{-1}$ and vertical scattering vector q-range of $-0.1\ nm^{-1} < q_V < 2.9\ nm^{-1}$. The X-ray beam was collimated to a spot size at the sample of approximately 200 μm × 200 μm. The images were recorded using the Pilatus 1 M detector (Dectris, Switzerland) with an exposure time of 10 s per image. Reference patterns to calibrate the q-scale were collected of silver-behenate (d-spacings of 5.838 nm). Samples were mounted on a 2-axis goniometer stage with 0.001° angular precision, allowing us to ensure an incidence angle of 0.04° for the measurements (determined by alignment of the specular reflection on the detector). The presented data were corrected for fluctuations of the primary intensity. Data treatment was done using the NIKA2D[83] (geometry correction and calibration) as well as GIXSGUI[84] (lattice indexing) software packages.

Optical Spectroscopy. For the PL measurements, the sample was mounted on an XYZ nanopositioning stage inside an evacuated liquid-helium coldfinger cryostat and cooled to 6 K. Nanocrystals were excited with a fiber-coupled excitation laser at a photon energy of 3.06 eV with pulses of 50 ps duration. A long working-distance, 100×, microscope objective with a numerical aperture of 0.7 was used for both excitation and detection, leading to a Gaussian excitation spot with a $1/e^2$ diameter of 1.4 μm. The emission was then dispersed in a 750 mm monochromator by a 3000 lines per mm grating and detected with a back-illuminated, cooled EMCCD camera.

For absorption and PL experiments reported in Figure 19, a custom-made setup, enabling both experiments to probe the same sample area, was used. The samples were placed on the coldfinger of a Janis CCS-150 closed-cycle optical refrigerator, allowing temperature variation within the 10−300 K range. Steady-state PL was excited by a 405 nm diode laser, focused onto a ∼2 μm diameter spot, via a Mitutoyo long working distance objective with 50× magnification and 0.55 numerical aperture. The emission was detected via the same objective, using a long-pass filter to block the excitation laser, while spectrally analyzed by a 0.75 m Acton750i Princeton spectrometer equipped with a 1024 × 256 pixels PIXIS charge-coupled device (CCD) camera. For absorption measurements, a tungsten-halogen white light source was coupled into a 600 μm core multimode fiber, and the output beam was focused onto the sample via the same microscope objective described above. The transmitted beam was coaxially collected and analyzed via the same combination of spectrometer and CCD described above.

Optical Properties of $CsPbBr_3$ NCs in Toluene. Optical absorption spectra were measured with Jasco V770 spectrometer in transmission mode. PL spectra were measured in a 90° configuration using Horiba Fluoromax-4P+ equipped with a photomultiplier tube and a monochromatized 150 W xenon lamp as an excitation source.

ASSOCIATED CONTENT

Supporting Information

including three Supplementary Video files. The Supporting Information is available free of charge at https://pubs.acs.org/doi/10.1021/acsnano.1c10702.

Video S1: Tomographic reconstruction of binary AlB_2-type SL comprising 5.3 nm $CsPbBr_3$ nanocubes and 15.2 nm $NaGdF_4$ spherical NCs (AVI)

https://doi.org/10.1021/acsnano.1c10702
ACS Nano 2022, 16, 7210−7232

Video S2: Tomographic reconstruction of binary CaC_2-type SL comprising 8.6 nm $CsPbBr_3$ nanocubes and 31.5 nm $NaGdF_4$ thick nanodisks (AVI)

GISAXS characterization of AlB_2-type SL; packing analysis of AlB_2-, AB_2- and b-ABO_6-type SLs; additional TEM characterization of NC building blocks and binary NC SLs (PDF)

Video S3: Tomographic reconstruction of binary ABO_3-type supraparticle comprising 8.6 nm $CsPbBr_3$ nanocubes and 18.6 nm $NaGdF_4$ spherical NCs (AVI)

AUTHOR INFORMATION

Corresponding Authors

Maksym V. Kovalenko − *Institute of Inorganic Chemistry, Department of Chemistry and Applied Biosciences, ETH Zürich, CH-8093 Zürich, Switzerland; Laboratory for Thin Films and Photovoltaics, Empa−Swiss Federal Laboratories for Materials Science and Technology, CH-8600 Dübendorf, Switzerland;* orcid.org/0000-0002-6396-8938; Email: mvkovalenko@ethz.ch

Maryna I. Bodnarchuk − *Institute of Inorganic Chemistry, Department of Chemistry and Applied Biosciences, ETH Zürich, CH-8093 Zürich, Switzerland; Laboratory for Thin Films and Photovoltaics, Empa−Swiss Federal Laboratories for Materials Science and Technology, CH-8600 Dübendorf, Switzerland;* orcid.org/0000-0001-6597-3266; Email: maryna.bodnarchuk@empa.ch

Authors

Ihor Cherniukh − *Institute of Inorganic Chemistry, Department of Chemistry and Applied Biosciences, ETH Zürich, CH-8093 Zürich, Switzerland; Laboratory for Thin Films and Photovoltaics, Empa−Swiss Federal Laboratories for Materials Science and Technology, CH-8600 Dübendorf, Switzerland;* orcid.org/0000-0001-7155-5095

Taras V. Sekh − *Institute of Inorganic Chemistry, Department of Chemistry and Applied Biosciences, ETH Zürich, CH-8093 Zürich, Switzerland; Laboratory for Thin Films and Photovoltaics, Empa−Swiss Federal Laboratories for Materials Science and Technology, CH-8600 Dübendorf, Switzerland*

Gabriele Rainò − *Institute of Inorganic Chemistry, Department of Chemistry and Applied Biosciences, ETH Zürich, CH-8093 Zürich, Switzerland; Laboratory for Thin Films and Photovoltaics, Empa−Swiss Federal Laboratories for Materials Science and Technology, CH-8600 Dübendorf, Switzerland;* orcid.org/0000-0002-2395-4937

Olivia J. Ashton − *Electron Microscopy Center, Empa−Swiss Federal Laboratories for Materials Science and Technology, CH-8600 Dübendorf, Switzerland;* orcid.org/0000-0002-0886-2110

Max Burian − *Swiss Light Source, Paul Scherrer Institute, 5232 Villigen PSI, Switzerland;* orcid.org/0000-0001-6728-6347

Alex Travesset − *Department of Physics and Astronomy and Ames Laboratory, Iowa State University, Ames, Iowa 50011, United States;* orcid.org/0000-0001-7030-9570

Modestos Athanasiou − *Experimental Condensed Matter Physics Laboratory, Department of Physics, University of Cyprus, 1678 Nicosia, Cyprus;* orcid.org/0000-0003-1684-9482

Andreas Manoli − *Experimental Condensed Matter Physics Laboratory, Department of Physics, University of Cyprus, 1678 Nicosia, Cyprus*

Rohit Abraham John − *Institute of Inorganic Chemistry, Department of Chemistry and Applied Biosciences, ETH Zürich, CH-8093 Zürich, Switzerland; Laboratory for Thin Films and Photovoltaics, Empa−Swiss Federal Laboratories for Materials Science and Technology, CH-8600 Dübendorf, Switzerland;* orcid.org/0000-0002-1709-0386

Mariia Svyrydenko − *Institute of Inorganic Chemistry, Department of Chemistry and Applied Biosciences, ETH Zürich, CH-8093 Zürich, Switzerland; Laboratory for Thin Films and Photovoltaics, Empa−Swiss Federal Laboratories for Materials Science and Technology, CH-8600 Dübendorf, Switzerland*

Viktoriia Morad − *Institute of Inorganic Chemistry, Department of Chemistry and Applied Biosciences, ETH Zürich, CH-8093 Zürich, Switzerland; Laboratory for Thin Films and Photovoltaics, Empa−Swiss Federal Laboratories for Materials Science and Technology, CH-8600 Dübendorf, Switzerland*

Yevhen Shynkarenko − *Institute of Inorganic Chemistry, Department of Chemistry and Applied Biosciences, ETH Zürich, CH-8093 Zürich, Switzerland; Laboratory for Thin Films and Photovoltaics, Empa−Swiss Federal Laboratories for Materials Science and Technology, CH-8600 Dübendorf, Switzerland*

Federico Montanarella − *Institute of Inorganic Chemistry, Department of Chemistry and Applied Biosciences, ETH Zürich, CH-8093 Zürich, Switzerland; Laboratory for Thin Films and Photovoltaics, Empa−Swiss Federal Laboratories for Materials Science and Technology, CH-8600 Dübendorf, Switzerland;* orcid.org/0000-0002-9057-7414

Denys Naumenko − *Institute of Inorganic Chemistry, Graz University of Technology, 8010 Graz, Austria*

Heinz Amenitsch − *Institute of Inorganic Chemistry, Graz University of Technology, 8010 Graz, Austria*

Grigorios Itskos − *Experimental Condensed Matter Physics Laboratory, Department of Physics, University of Cyprus, 1678 Nicosia, Cyprus;* orcid.org/0000-0003-3971-3801

Rainer F. Mahrt − *IBM Research Europe−Zurich, CH-8803 Rüschlikon, Switzerland;* orcid.org/0000-0002-9772-1490

Thilo Stöferle − *IBM Research Europe−Zurich, CH-8803 Rüschlikon, Switzerland;* orcid.org/0000-0003-0612-7195

Rolf Erni − *Electron Microscopy Center, Empa−Swiss Federal Laboratories for Materials Science and Technology, CH-8600 Dübendorf, Switzerland;* orcid.org/0000-0003-2391-5943

Complete contact information is available at: https://pubs.acs.org/10.1021/acsnano.1c10702

Notes

The authors declare no competing financial interest.

ACKNOWLEDGMENTS

This work was supported by the Swiss National Science Foundation (grant number 200021_192308, project Q-Light) and, in part, by the European Union through Horizon 2020 Research and Innovation Programme (ERC CoG Grant, grant agreement number 819740, project SCALE-HALO) and by

the Air Force Office of Scientific Research under award number FA8655-21-1-7013. The authors acknowledge support by the Research and Innovation Foundation of Cyprus, under the "New Strategic Infrastructure Units-Young Scientists" Program, grant agreement number "INFRASTRUCTURES/1216/0004", Acronym "NANOSONICS". M.A. acknowledges financial support by the European Union's Horizon 2020 research and innovation programme under the Marie Skłodowska-Curie grant agreement number 831690. We acknowledge the funding received from EU-H2020 under grant agreement number 654360 supporting the Transnational Access Activity within the framework NFFA-Europe to the TUG's ELETTRA SAXS beamline of CERIC–ERIC. A.T. acknowledges the funding received from the National Science Foundation (USA) DMR-CMMT 1606336. F.M. acknowledges support from ETH Zürich via the ETH Postdoctoral Fellowship (FEL-15 18-2) and from the Marie Skłodowska-Curie Actions COFUND Program. We thank M. Rossell for the high-resolution HAADF-STEM image used in Figure 1. The authors are grateful for the use of facilities at the Empa Electron Microscopy Center.

REFERENCES

(1) Boles, M. A.; Engel, M.; Talapin, D. V. Self-Assembly of Colloidal Nanocrystals: From Intricate Structures to Functional Materials. *Chem. Rev.* **2016**, *116*, 11220–11289.
(2) Tan, R.; Zhu, H.; Cao, C.; Chen, O. Multi-Component Superstructures Self-Assembled from Nanocrystal Building Blocks. *Nanoscale* **2016**, *8*, 9944–9961.
(3) Urban, J. J.; Talapin, D. V.; Shevchenko, E. V.; Kagan, C. R.; Murray, C. B. Synergism in Binary Nanocrystal Superlattices Leads to Enhanced *P*-Type Conductivity in Self-Assembled PbTe/Ag_2Te Thin Films. *Nat. Mater.* **2007**, *6*, 115–121.
(4) Chen, J.; Ye, X.; Oh, S. J.; Kikkawa, J. M.; Kagan, C. R.; Murray, C. B. Bistable Magnetoresistance Switching in Exchange-Coupled $CoFe_2O_4$-Fe_3O_4 Binary Nanocrystal Superlattices by Self-Assembly and Thermal Annealing. *ACS Nano* **2013**, *7*, 1478–1486.
(5) Ye, X.; Chen, J.; Diroll, B. T.; Murray, C. B. Tunable Plasmonic Coupling in Self-Assembled Binary Nanocrystal Superlattices Studied by Correlated Optical Microspectrophotometry and Electron Microscopy. *Nano Lett.* **2013**, *13*, 1291–1297.
(6) Talapin, D. V.; Shevchenko, E. V.; Kornowski, A.; Gaponik, N.; Haase, M.; Rogach, A. L.; Weller, H. A New Approach to Crystallization of CdSe Nanoparticles into Ordered Three-Dimensional Superlattices. *Adv. Mater.* **2001**, *13*, 1868–1871.
(7) Bodnarchuk, M. I.; Kovalenko, M. V.; Heiss, W.; Talapin, D. V. Energetic and Entropic Contributions to Self-Assembly of Binary Nanocrystal Superlattices: Temperature as the Structure-Directing Factor. *J. Am. Chem. Soc.* **2010**, *132*, 11967–11977.
(8) Boles, M. A.; Talapin, D. V. Self-Assembly of Tetrahedral CdSe Nanocrystals: Effective "Patchiness" *via* Anisotropic Steric Interaction. *J. Am. Chem. Soc.* **2014**, *136*, 5868–5871.
(9) Dong, A.; Chen, J.; Vora, P. M.; Kikkawa, J. M.; Murray, C. B. Binary Nanocrystal Superlattice Membranes Self-Assembled at the Liquid-Air Interface. *Nature* **2010**, *466*, 474–477.
(10) Paik, T.; Yun, H.; Fleury, B.; Hong, S. H.; Jo, P. S.; Wu, Y.; Oh, S. J.; Cargnello, M.; Yang, H.; Murray, C. B.; Kagan, C. R. Hierarchical Materials Design by Pattern Transfer Printing of Self-Assembled Binary Nanocrystal Superlattices. *Nano Lett.* **2017**, *17*, 1387–1394.
(11) Ye, X.; Collins, J. E.; Kang, Y.; Chen, J.; Chen, D. T.; Yodh, A. G.; Murray, C. B. Morphologically Controlled Synthesis of Colloidal Upconversion Nanophosphors and Their Shape-Directed Self-Assembly. *Proc. Natl. Acad. Sci. U. S. A.* **2010**, *107*, 22430–22435.
(12) Wang, P. P.; Qiao, Q.; Zhu, Y.; Ouyang, M. Colloidal Binary Supracrystals with Tunable Structural Lattices. *J. Am. Chem. Soc.* **2018**, *140*, 9095–9098.
(13) de Nijs, B.; Dussi, S.; Smallenburg, F.; Meeldijk, J. D.; Groenendijk, D. J.; Filion, L.; Imhof, A.; van Blaaderen, A.; Dijkstra, M. Entropy-driven formation of large icosahedral colloidal clusters by spherical confinement. *Nat. Mater.* **2015**, *14*, 56–60.
(14) Yu, Y.; Yu, D.; Orme, C. A. Reversible, Tunable, Electric-Field Driven Assembly of Silver Nanocrystal Superlattices. *Nano Lett.* **2017**, *17*, 3862–3869.
(15) Singh, G.; Chan, H.; Baskin, A.; Gelman, E.; Repnin, N.; Kral, P.; Klajn, R. Self-Assembly of Magnetite Nanocubes into Helical Superstructures. *Science* **2014**, *345*, 1149–1153.
(16) Bishop, K. J.; Wilmer, C. E.; Soh, S.; Grzybowski, B. A. Nanoscale Forces and Their Uses in Self-Assembly. *Small* **2009**, *5*, 1600–1630.
(17) Murray, C. B.; Kagan, C. R.; Bawendi, M. G. Self-Organization of CdSe Nanocrystallites into Three-Dimensional Quantum Dot Superlattices. *Science* **1995**, *270*, 1335–1338.
(18) Shevchenko, E. V.; Talapin, D. V.; Kotov, N. A.; O'Brien, S.; Murray, C. B. Structural Diversity in Binary Nanoparticle Superlattices. *Nature* **2006**, *439*, 55–59.
(19) Boles, M. A.; Talapin, D. V. Many-Body Effects in Nanocrystal Superlattices: Departure from Sphere Packing Explains Stability of Binary Phases. *J. Am. Chem. Soc.* **2015**, *137*, 4494–4502.
(20) Coropceanu, I.; Boles, M. A.; Talapin, D. V. Systematic Mapping of Binary Nanocrystal Superlattices: The Role of Topology in Phase Selection. *J. Am. Chem. Soc.* **2019**, *141*, 5728–5740.
(21) Landman, U.; Luedtke, W. D. Small Is Different: Energetic, Structural, Thermal, and Mechanical Properties of Passivated Nanocluster Assemblies. *Faraday Discuss.* **2004**, *125*, 1–22.
(22) Deng, K.; Luo, Z.; Tan, L.; Quan, Z. Self-Assembly of Anisotropic Nanoparticles into Functional Superstructures. *Chem. Soc. Rev.* **2020**, *49*, 6002–6038.
(23) Glotzer, S. C.; Solomon, M. J. Anisotropy of Building Blocks and Their Assembly into Complex Structures. *Nat. Mater.* **2007**, *6*, 557–562.
(24) Millan, J. A.; Ortiz, D.; van Anders, G.; Glotzer, S. C. Self-Assembly of Archimedean Tilings with Enthalpically and Entropically Patchy Polygons. *ACS Nano* **2014**, *8*, 2918–2928.
(25) van Anders, G.; Klotsa, D.; Ahmed, N. K.; Engel, M.; Glotzer, S. C. Understanding Shape Entropy through Local Dense Packing. *Proc. Natl. Acad. Sci. U. S. A.* **2014**, *111*, E4812–E4821.
(26) Demortiere, A.; Launois, P.; Goubet, N.; Albouy, P. A.; Petit, C. Shape-Controlled Platinum Nanocubes and Their Assembly into Two-Dimensional and Three-Dimensional Superlattices. *J. Phys. Chem. B* **2008**, *112*, 14583–14592.
(27) Quan, Z.; Loc, W. S.; Lin, C.; Luo, Z.; Yang, K.; Wang, Y.; Wang, H.; Wang, Z.; Fang, J. Tilted Face-Centered-Cubic Supercrystals of PbS Nanocubes. *Nano Lett.* **2012**, *12*, 4409–4413.
(28) Disch, S.; Wetterskog, E.; Hermann, R. P.; Salazar-Alvarez, G.; Busch, P.; Bruckel, T.; Bergstrom, L.; Kamali, S. Shape Induced Symmetry in Self-Assembled Mesocrystals of Iron Oxide Nanocubes. *Nano Lett.* **2011**, *11*, 1651–1656.
(29) Disch, S.; Wetterskog, E.; Hermann, R. P.; Korolkov, D.; Busch, P.; Boesecke, P.; Lyon, O.; Vainio, U.; Salazar-Alvarez, G.; Bergstrom, L.; Bruckel, T. Structural Diversity in Iron Oxide Nanoparticle Assemblies as Directed by Particle Morphology and Orientation. *Nanoscale* **2013**, *5*, 3969–3975.
(30) Sanchez-Iglesias, A.; Grzelczak, M.; Perez-Juste, J.; Liz-Marzan, L. M. Binary Self-Assembly of Gold Nanowires with Nanospheres and Nanorods. *Angew. Chem., Int. Ed. Engl.* **2010**, *49*, 9985–9989.
(31) Paik, T.; Ko, D. K.; Gordon, T. R.; Doan-Nguyen, V.; Murray, C. B. Studies of Liquid Crystalline Self-Assembly of GdF_3 Nanoplates by In-Plane, Out-of-Plane SAXS. *ACS Nano* **2011**, *5*, 8322–8330.
(32) Nagaoka, Y.; Wang, T.; Lynch, J.; LaMontagne, D.; Cao, Y. C. Binary Assembly of Colloidal Semiconductor Nanorods with Spherical Metal Nanoparticles. *Small* **2012**, *8*, 843–846.
(33) Ye, X.; Millan, J. A.; Engel, M.; Chen, J.; Diroll, B. T.; Glotzer, S. C.; Murray, C. B. Shape Alloys of Nanorods and Nanospheres from Self-Assembly. *Nano Lett.* **2013**, *13*, 4980–4988.

https://doi.org/10.1021/acsnano.1c10702
ACS Nano 2022, 16, 7210–7232

(34) Ming, T.; Kou, X.; Chen, H.; Wang, T.; Tam, H. L.; Cheah, K. W.; Chen, J. Y.; Wang, J. Ordered Gold Nanostructure Assemblies Formed by Droplet Evaporation. *Angew. Chem., Int. Ed. Engl.* **2008**, *47*, 9685−9690.
(35) Castelli, A.; de Graaf, J.; Prato, M.; Manna, L.; Arciniegas, M. P. Tic-Tac-Toe Binary Lattices from the Interfacial Self-Assembly of Branched and Spherical Nanocrystals. *ACS Nano* **2016**, *10*, 4345−4353.
(36) Paik, T.; Murray, C. B. Shape-Directed Binary Assembly of Anisotropic Nanoplates: A Nanocrystal Puzzle with Shape-Complementary Building Blocks. *Nano Lett.* **2013**, *13*, 2952−2956.
(37) Paik, T.; Diroll, B. T.; Kagan, C. R.; Murray, C. B. Binary and Ternary Superlattices Self-Assembled from Colloidal Nanodisks and Nanorods. *J. Am. Chem. Soc.* **2015**, *137*, 6662−6669.
(38) Elbert, K. C.; Zygmunt, W.; Vo, T.; Vara, C. M.; Rosen, D. J.; Krook, N. M.; Glotzer, S. C.; Murray, C. B. Anisotropic Nanocrystal Shape and Ligand Design for Co-Assembly. *Sci. Adv.* **2021**, *7*, No. eabf9402.
(39) Protesescu, L.; Yakunin, S.; Bodnarchuk, M. I.; Krieg, F.; Caputo, R.; Hendon, C. H.; Yang, R. X.; Walsh, A.; Kovalenko, M. V. Nanocrystals of Cesium Lead Halide Perovskites ($CsPbX_3$, X = Cl, Br, and I): Novel Optoelectronic Materials Showing Bright Emission with Wide Color Gamut. *Nano Lett.* **2015**, *15*, 3692−3696.
(40) Kovalenko, M. V.; Protesescu, L.; Bodnarchuk, M. I. Properties and Potential Optoelectronic Applications of Lead Halide Perovskite Nanocrystals. *Science* **2017**, *358*, 745−750.
(41) Akkerman, Q. A.; Rainò, G.; Kovalenko, M. V.; Manna, L. Genesis, Challenges and Opportunities for Colloidal Lead Halide Perovskite Nanocrystals. *Nat. Mater.* **2018**, *17*, 394−405.
(42) Dey, A.; Ye, J.; De, A.; Debroye, E.; Ha, S. K.; Bladt, E.; Kshirsagar, A. S.; Wang, Z.; Yin, J.; Wang, Y.; Quan, L. N.; Yan, F.; Gao, M.; Li, X.; Shamsi, J.; Debnath, T.; Cao, M.; Scheel, M. A.; Kumar, S.; Steele, J. A.; Gerhard, M.; Chouhan, L.; Xu, K.; Wu, X. G.; Li, Y.; Zhang, Y.; Dutta, A.; Han, C.; Vincon, I.; Rogach, A. L.; Nag, A.; Samanta, A.; Korgel, B. A.; Shih, C. J.; Gamelin, D. R.; Son, D. H.; Zeng, H.; Zhong, H.; Sun, H.; Demir, H. V.; Scheblykin, I. G.; Mora-Sero, I.; Stolarczyk, J. K.; Zhang, J. Z.; Feldmann, J.; Hofkens, J.; Luther, J. M.; Perez-Prieto, J.; Li, L.; Manna, L.; Bodnarchuk, M. I.; Kovalenko, M. V.; Roeffaers, M. B. J.; Pradhan, N.; Mohammed, O. F.; Bakr, O. M.; Yang, P.; Muller-Buschbaum, P.; Kamat, P. V.; Bao, Q.; Zhang, Q.; Krahne, R.; Galian, R. E.; Stranks, S. D.; Bals, S.; Biju, V.; Tisdale, W. A.; Yan, Y.; Hoye, R. L. Z.; Polavarapu, L. State of the Art and Prospects for Halide Perovskite Nanocrystals. *ACS Nano* **2021**, *15*, 10775−10981.
(43) Lu, M.; Zhang, Y.; Wang, S.; Guo, J.; Yu, W. W.; Rogach, A. L. Metal Halide Perovskite Light-Emitting Devices: Promising Technology for Next-Generation Displays. *Adv. Funct. Mater.* **2019**, *29*, 1902008.
(44) Quan, L. N.; Rand, B. P.; Friend, R. H.; Mhaisalkar, S. G.; Lee, T. W.; Sargent, E. H. Perovskites for Next-Generation Optical Sources. *Chem. Rev.* **2019**, *119*, 7444−7477.
(45) Utzat, H.; Sun, W.; Kaplan, A. E. K.; Krieg, F.; Ginterseder, M.; Spokoyny, B.; Klein, N. D.; Shulenberger, K. E.; Perkinson, C. F.; Kovalenko, M. V.; Bawendi, M. G. Coherent Single-Photon Emission From Colloidal Lead Halide Perovskite Quantum Dots. *Science* **2019**, *363*, 1068−1072.
(46) Raino, G.; Nedelcu, G.; Protesescu, L.; Bodnarchuk, M. I.; Kovalenko, M. V.; Mahrt, R. F.; Stoferle, T. Single Cesium Lead Halide Perovskite Nanocrystals at Low Temperature: Fast Single-Photon Emission, Reduced Blinking, and Exciton Fine Structure. *ACS Nano* **2016**, *10*, 2485−2490.
(47) Almeida, G.; Goldoni, L.; Akkerman, Q.; Dang, Z.; Khan, A. H.; Marras, S.; Moreels, I.; Manna, L. Role of Acid-Base Equilibria in the Size, Shape, and Phase Control of Cesium Lead Bromide Nanocrystals. *ACS Nano* **2018**, *12*, 1704−1711.
(48) Hudait, B.; Dutta, S. K.; Patra, A.; Nasipuri, D.; Pradhan, N. Facets Directed Connecting Perovskite Nanocrystals. *J. Am. Chem. Soc.* **2020**, *142*, 7207−7217.
(49) Bera, S.; Behera, R. K.; Pradhan, N. alpha-Halo Ketone for Polyhedral Perovskite Nanocrystals: Evolutions, Shape Conversions, Ligand Chemistry, and Self-Assembly. *J. Am. Chem. Soc.* **2020**, *142*, 20865−20874.
(50) Kovalenko, M. V.; Bodnarchuk, M. I. Lead Halide Perovskite Nanocrystals: From Discovery to Self-Assembly and Applications. *Chimia* **2017**, *71*, 461−470.
(51) Nagaoka, Y.; Hills-Kimball, K.; Tan, R.; Li, R.; Wang, Z.; Chen, O. Nanocube Superlattices of Cesium Lead Bromide Perovskites and Pressure-Induced Phase Transformations at Atomic and Mesoscale Levels. *Adv. Mater.* **2017**, *29*, 1606666.
(52) van der Burgt, J. S.; Geuchies, J. J.; van der Meer, B.; Vanrompay, H.; Zanaga, D.; Zhang, Y.; Albrecht, W.; Petukhov, A. V.; Filion, L.; Bals, S.; Swart, I.; Vanmaekelbergh, D. Cuboidal Supraparticles Self-Assembled from Cubic $CsPbBr_3$ Perovskite Nanocrystals. *J. Phys. Chem. C* **2018**, *122*, 15706−15712.
(53) Rainò, G.; Becker, M. A.; Bodnarchuk, M. I.; Mahrt, R. F.; Kovalenko, M. V.; Stöferle, T. Superfluorescence From Lead Halide Perovskite Quantum Dot Superlattices. *Nature* **2018**, *563*, 671−675.
(54) Baranov, D.; Toso, S.; Imran, M.; Manna, L. Investigation into the Photoluminescence Red Shift in Cesium Lead Bromide Nanocrystal Superlattices. *J. Phys. Chem. Lett.* **2019**, *10*, 655−660.
(55) Tong, Y.; Yao, E. P.; Manzi, A.; Bladt, E.; Wang, K.; Doblinger, M.; Bals, S.; Muller-Buschbaum, P.; Urban, A. S.; Polavarapu, L.; Feldmann, J. Spontaneous Self-Assembly of Perovskite Nanocrystals into Electronically Coupled Supercrystals: Toward Filling the Green Gap. *Adv. Mater.* **2018**, *30*, No. 1801117.
(56) Imran, M.; Ijaz, P.; Baranov, D.; Goldoni, L.; Petralanda, U.; Akkerman, Q.; Abdelhady, A. L.; Prato, M.; Bianchini, P.; Infante, I.; Manna, L. Shape-Pure, Nearly Monodispersed $CsPbBr_3$ Nanocubes Prepared Using Secondary Aliphatic Amines. *Nano Lett.* **2018**, *18*, 7822−7831.
(57) Toso, S.; Baranov, D.; Giannini, C.; Marras, S.; Manna, L. Wide-Angle X-ray Diffraction Evidence of Structural Coherence in $CsPbBr_3$ Nanocrystal Superlattices. *ACS Mater. Lett.* **2019**, *1*, 272−276.
(58) Cherniukh, I.; Rainò, G.; Stöferle, T.; Burian, M.; Travesset, A.; Naumenko, D.; Amenitsch, H.; Erni, R.; Mahrt, R. F.; Bodnarchuk, M. I.; Kovalenko, M. V. Perovskite-Type Superlattices from Lead Halide Perovskite Nanocubes. *Nature* **2021**, *593*, 535−542.
(59) Cherniukh, I.; Raino, G.; Sekh, T. V.; Zhu, C.; Shynkarenko, Y.; John, R. A.; Kobiyama, E.; Mahrt, R. F.; Stoferle, T.; Erni, R.; Kovalenko, M. V.; Bodnarchuk, M. I. Shape-Directed Co-Assembly of Lead Halide Perovskite Nanocubes with Dielectric Nanodisks into Binary Nanocrystal Superlattices. *ACS Nano* **2021**, *15*, 16488−16500.
(60) Bertolotti, F.; Nedelcu, G.; Vivani, A.; Cervellino, A.; Masciocchi, N.; Guagliardi, A.; Kovalenko, M. V. Crystal Structure, Morphology, and Surface Termination of Cyan-Emissive, Six-Monolayers-Thick $CsPbBr_3$ Nanoplatelets from X-Ray Total Scattering. *ACS Nano* **2019**, *13*, 14294−14307.
(61) Dong, Y.; Qiao, T.; Kim, D.; Parobek, D.; Rossi, D.; Son, D. H. Precise Control of Quantum Confinement in Cesium Lead Halide Perovskite Quantum Dots *via* Thermodynamic Equilibrium. *Nano Lett.* **2018**, *18*, 3716−3722.
(62) Bodnarchuk, M. I.; Boehme, S. C.; Ten Brinck, S.; Bernasconi, C.; Shynkarenko, Y.; Krieg, F.; Widmer, R.; Aeschlimann, B.; Gunther, D.; Kovalenko, M. V.; Infante, I. Rationalizing and Controlling the Surface Structure and Electronic Passivation of Cesium Lead Halide Nanocrystals. *ACS Energy Lett.* **2019**, *4*, 63−74.
(63) Park, J.; An, K.; Hwang, Y.; Park, J. G.; Noh, H. J.; Kim, J. Y.; Park, J. H.; Hwang, N. M.; Hyeon, T. Ultra-Large-Scale Syntheses of Monodisperse Nanocrystals. *Nat. Mater.* **2004**, *3*, 891−895.
(64) Travesset, A. Topological Structure Prediction in Binary Nanoparticle Superlattices. *Soft Matter* **2017**, *13*, 147−157.
(65) Boles, M. A.; Talapin, D. V. Binary Assembly of PbS and Au Nanocrystals: Patchy PbS Surface Ligand Coverage Stabilizes the CuAu Superlattice. *ACS Nano* **2019**, *13*, 5375−5384.

https://doi.org/10.1021/acsnano.1c10702
ACS Nano 2022, 16, 7210−7232

(66) Zhuang, J.; Wu, H.; Yang, Y.; Cao, Y. C. Supercrystalline Colloidal Particles from Artificial Atoms. *J. Am. Chem. Soc.* **2007**, *129*, 14166−14167.
(67) Zhuang, J.; Wu, H.; Yang, Y.; Cao, Y. C. Controlling Colloidal Superparticle Growth through Solvophobic Interactions. *Angew. Chem., Int. Ed.* **2008**, *47*, 2208−2212.
(68) Yang, Y.; Wang, B.; Shen, X.; Yao, L.; Wang, L.; Chen, X.; Xie, S.; Li, T.; Hu, J.; Yang, D.; Dong, A. Scalable Assembly of Crystalline Binary Nanocrystal Superparticles and Their Enhanced Magnetic and Electrochemical Properties. *J. Am. Chem. Soc.* **2018**, *140*, 15038−15047.
(69) Kister, T.; Mravlak, M.; Schilling, T.; Kraus, T. Pressure-Controlled Formation of Crystalline, Janus, and Core-Shell Supraparticles. *Nanoscale* **2016**, *8*, 13377−13384.
(70) Tang, Y.; Gomez, L.; Lesage, A.; Marino, E.; Kodger, T. E.; Meijer, J. M.; Kolpakov, P.; Meng, J.; Zheng, K.; Gregorkiewicz, T.; Schall, P. Highly Stable Perovskite Supercrystals via Oil-in-Oil Templating. *Nano Lett.* **2020**, *20*, 5997−6004.
(71) Wang, D.; van der Wee, E. B.; Zanaga, D.; Altantzis, T.; Wu, Y.; Dasgupta, T.; Dijkstra, M.; Murray, C. B.; Bals, S.; van Blaaderen, A. Quantitative 3D Real-Space Analysis of Laves Phase Supraparticles. *Nat. Commun.* **2021**, *12*, 3980.
(72) Montanarella, F.; Geuchies, J. J.; Dasgupta, T.; Prins, P. T.; van Overbeek, C.; Dattani, R.; Baesjou, P.; Dijkstra, M.; Petukhov, A. V.; van Blaaderen, A.; Vanmaekelbergh, D. Crystallization of Nanocrystals in Spherical Confinement Probed by in Situ X-ray Scattering. *Nano Lett.* **2018**, *18*, 3675−3681.
(73) Becker, M. A.; Vaxenburg, R.; Nedelcu, G.; Sercel, P. C.; Shabaev, A.; Mehl, M. J.; Michopoulos, J. G.; Lambrakos, S. G.; Bernstein, N.; Lyons, J. L.; Stöferle, T.; Mahrt, R. F.; Kovalenko, M. V.; Norris, D. J.; Rainò, G.; Efros, A. L. Bright Triplet Excitons in Caesium Lead Halide Perovskites. *Nature* **2018**, *553*, 189−193.
(74) Becker, M. A.; Scarpelli, L.; Nedelcu, G.; Raino, G.; Masia, F.; Borri, P.; Stoferle, T.; Kovalenko, M. V.; Langbein, W.; Mahrt, R. F. Long Exciton Dephasing Time and Coherent Phonon Coupling in $CsPbBr_2Cl$ Perovskite Nanocrystals. *Nano Lett.* **2018**, *18*, 7546−7551.
(75) Hestand, N. J.; Spano, F. C. Expanded Theory of H- and J-Molecular Aggregates: The Effects of Vibronic Coupling and Intermolecular Charge Transfer. *Chem. Rev.* **2018**, *118*, 7069−7163.
(76) Yaffe, O.; Guo, Y.; Tan, L. Z.; Egger, D. A.; Hull, T.; Stoumpos, C. C.; Zheng, F.; Heinz, T. F.; Kronik, L.; Kanatzidis, M. G.; Owen, J. S.; Rappe, A. M.; Pimenta, M. A.; Brus, L. E. Local Polar Fluctuations in Lead Halide Perovskite Crystals. *Phys. Rev. Lett.* **2017**, *118*, 136001.
(77) Lanigan-Atkins, T.; He, X.; Krogstad, M. J.; Pajerowski, D. M.; Abernathy, D. L.; Xu, G.; Xu, Z.; Chung, D. Y.; Kanatzidis, M. G.; Rosenkranz, S.; Osborn, R.; Delaire, O. Two-Dimensional Overdamped Fluctuations of the Soft Perovskite Lattice in $CsPbBr_3$. *Nat. Mater.* **2021**, *20*, 977−983.
(78) Baranov, D.; Fieramosca, A.; Yang, R. X.; Polimeno, L.; Lerario, G.; Toso, S.; Giansante, C.; Giorgi, M.; Tan, L. Z.; Sanvitto, D.; Manna, L. Aging of Self-Assembled Lead Halide Perovskite Nanocrystal Superlattices: Effects on Photoluminescence and Energy Transfer. *ACS Nano* **2021**, *15*, 650−664.
(79) De Roo, J.; Ibanez, M.; Geiregat, P.; Nedelcu, G.; Walravens, W.; Maes, J.; Martins, J. C.; Van Driessche, I.; Kovalenko, M. V.; Hens, Z. Highly Dynamic Ligand Binding and Light Absorption Coefficient of Cesium Lead Bromide Perovskite Nanocrystals. *ACS Nano* **2016**, *10*, 2071−2081.
(80) Ibanez, M.; Korkosz, R. J.; Luo, Z.; Riba, P.; Cadavid, D.; Ortega, S.; Cabot, A.; Kanatzidis, M. G. Electron Doping in Bottom-Up Engineered Thermoelectric Nanomaterials through HCl-Mediated Ligand Displacement. *J. Am. Chem. Soc.* **2015**, *137*, 4046−4049.
(81) Kremer, J. R.; Mastronarde, D. N.; McIntosh, J. R. Computer Visualization of Three-Dimensional Image Data Using IMOD. *J. Struct. Biol.* **1996**, *116*, 71−76.
(82) Amenitsch, H.; Bernstorff, S.; Laggner, P. High-Flux Beamline for Small-Angle X-Ray Scattering at ELETTRA. *Rev. Sci. Instrum.* **1995**, *66*, 1624−1626.
(83) Ilavsky, J. Nika: Software for Two-Dimensional Data Reduction. *J. Appl. Crystallogr.* **2012**, *45*, 324−328.
(84) Jiang, Z. GIXSGUI: a MATLAB Toolbox for Grazing-Incidence X-ray Scattering Data Visualization and Reduction, and Indexing of Buried Three-Dimensional Periodic Nanostructured Films. *J. Appl. Crystallogr.* **2015**, *48*, 917−926.

https://doi.org/10.1021/acsnano.1c10702
ACS Nano 2022, 16, 7210−7232